

1 **Evolution of Cloud Droplet Temperature and Lifetime in**
2 **Spatiotemporally Varying Subsaturated Environments with**
3 **Implications for Ice Nucleation at Cloud Edges**
4

5 Puja Roy^{1,2}, Robert M. Rauber¹, Larry Di Girolamo¹
6

7 ¹Department of Climate, Meteorology & Atmospheric Sciences, University of Illinois Urbana-Champaign, USA

8 ²Research Applications Laboratory, NSF National Center for Atmospheric Research, USA
9

10 *Correspondence to:* Puja Roy (pujaroy@ucar.edu)

11
12 **Abstract.** Ice formation mechanisms in generating cells near stratiform cloud-tops, where mixing and entrainment
13 occurs in the presence of supercooled water droplets, remain poorly understood. Supercooled cloud droplet
14 temperature and lifetime may impact heterogeneous ice nucleation through contact and immersion freezing; however,
15 modeling studies normally assume droplet temperature to be spatially uniform and equal to the ambient temperature.
16 Here, we present a first-of-its-kind quantitative investigation of the temperature and lifetime of evaporating droplets,
17 considering internal thermal gradients within the droplet as well as thermal and vapor density gradients in the
18 surrounding air. Our approach employs solving the Navier-Stokes and continuity equations, coupled with heat and
19 vapor transport, using an advanced numerical model. For typical ranges of cloud droplet sizes and environmental
20 conditions, the droplet internal thermal gradients dissipate quickly (≤ 0.3 s) when droplets are introduced to new
21 subsaturated environments. However, the magnitude of droplet cooling is much greater than estimated from past
22 studies of droplet evaporation, especially for drier environments. For example, for an environment with pressure of
23 500 hPa, and ambient temperature far from the droplet of -5°C , the droplet temperature reduction can be as high as
24 24, 11, and 5°C for initial ambient relative humidities of 10%, 40%, and 70% respectively. Droplet lifetimes are found
25 to be tens of seconds longer compared to previous estimates due to weaker evaporation rates because of lower droplet
26 surface temperatures. Using these new end-of-lifetime droplet temperatures, the enhancement in activation of ice-
27 nucleating particles predicted by current ice nucleation parameterization schemes is discussed.

30 **1 Introduction**

31
32 Ice formation often occurs near cloud tops of stratiform clouds where ice-generating cells (AMS 2024) are frequently
33 found in a variety of cold, cloudy environments (Plummer et al., 2014; Ramelli et al., 2021). These cells play a crucial
34 role in primary ice nucleation and growth (Tessendorf et al., 2015). Evidence of mixing and entrainment and the
35 presence of supercooled liquid water within and between the highly turbulent cells has been observed (Plummer et al.,
36 2014; Wang et al., 2020; Zaremba et al., 2024). Within regions of entrainment and mixing at cloud boundaries, cloud
37 droplets are exposed to subsaturated environments and undergo evaporation that leads to droplet temperatures that
38 could be several degrees lower than that of the ambient environment (Kinzer and Gunn, 1951; Watts, 1971; Roy et
39 al., 2023). However, in modeling cloud microphysical processes, the difference in temperature between the cloud
40 droplets and their environment is generally assumed to be negligible (Pruppacher and Klett, 1997), i.e., the droplets'
41 temperatures are approximated to be the same as that of their ambient environment. This assumption is reasonable for
42 cloud droplets inside the cloud but breaks down within entrainment and mixing zones at cloud boundaries and may
43 lead to uncertainties in the numerical simulations of microphysical processes. Cloud droplet temperatures affect the
44 calculated droplet diffusional growth or evaporation rates (Roach 1976; Srivastava and Coen 1992; Marquis and
45 Harrington 2005; Roy et al., 2023), and droplet lifetimes (Roy et al., 2023), radiative effects via temperature-dependent
46 refractive indices (Rowe et al. 2020), and ice formation via pathways that require supercooled liquid water droplets,
47 such as contact nucleation (Young, 1974), immersion freezing (Szakáll et al., 2021), and homogeneous nucleation
48 (Khvorostyanov and Sassen, 1998; Khain and Pinsky, 2018). These uncertainties can propagate into microphysical
49 parameterization schemes, leading to possible inadequate representation of mixed-phase cloud properties across
50 various scales (e.g., Large Eddy Simulations (LES), Cloud Resolving Models (CRM), Climate Models), impacting
51 predictions of precipitation or climate change.

52
53 Several studies have highlighted the special importance of the air-water interface of the water droplet during ice
54 nucleation. Many experimental and theoretical studies have suggested that ice initiation occurs at the droplet surface
55 (Tabazadeh et al., 2002a; Tabazadeh et al., 2002b; Djikaev et al., 2002; Satoh et al. 2002; Shaw et al., 2005) and the
56 interface thermodynamically favors the contact mode over the immersion freezing mode (Djikaev and Ruckenstein,
57 2008). Based on their laboratory observations, Tabazadeh et al., (2002a) suggested that homogeneous nucleation of
58 nitric acid dihydrate (NAD) and nitric acid trihydrate (NAT) particles within aqueous nitric acid droplets primarily
59 occurs at the droplet surface. This leads to the hypothesis that phase transformations in atmospheric aerosols may
60 predominantly be surface-based (Tabazadeh et al., 2002b), challenging the traditional theory of homogeneous
61 crystallization where freezing begins inside the volume of the droplet (Volmer, 1939). Satoh et al. (2002) studied
62 cooling and freezing in water droplets due to evaporation in an evacuated chamber and found that droplets rapidly
63 froze with significant supercooling, with the freezing initiated from the droplet surface. Studies employing molecular
64 dynamics simulations (Chushak et al., 1999, 2000) and thermodynamic calculations (Djikaev et al., 2002) additionally
65 corroborate that a crystalline nucleus preferentially forms at the droplet surface rather than within the bulk droplet
66 volume. Laboratory observations from Shaw et al., (2005) reveal that freezing temperatures are 4-5 K higher when an

67 ice-forming nucleus is closer to the surface of a supercooled water droplet compared to when it's immersed within the
68 droplet. They found that the nucleation rate at the water surface is significantly higher (by a factor of 10^{10}) than in the
69 bulk droplet, indicating that the free energy required for critical ice germ formation decreases when near the air-water
70 interface, and the jump frequency of molecules from the liquid to the solid phase may be significantly enhanced at the
71 interface. Lü et al., (2005) conducted ice nucleation experiments with acoustically levitated supercooled water
72 droplets. Using statistical analyses of nucleation rates, they found that ice nucleation predominantly initiates in the
73 vicinity of the droplet surface. Therefore, given the importance of the droplet surface in ice nucleation and since
74 evaporation is a surface phenomenon, in the quest to better understand the physical mechanisms responsible for
75 primary ice nucleation, it is important to accurately investigate the thermal evolution of the evaporating droplet surface
76 as well as the internal thermal gradients within the supercooled droplet, as ice nucleation is highly temperature
77 dependent.

78
79 Droplet condensation or evaporation results from vapor density gradients between the surface of the droplet and the
80 ambient environment. The solution to determine the rate of droplet growth or decay was first derived by Maxwell
81 (1890), with an alternative approximate solution presented by Mason (1971) which has since appeared in several
82 textbooks (e.g. Eq. 7.18 of Rogers and Yau, 1989; Eq. 13-28 of Pruppacher and Klett, 1997). The vapor density at the
83 droplet surface is a sensitive function of the temperature at the drop surface. For simplicity, cloud models, while
84 computing the growth/decay rates of cloud droplets, eliminate the use of droplet temperature from the equations by
85 assuming the saturation vapor density difference as a linear function of temperature difference between the droplet
86 and ambient environment (e.g. Vaillancourt et al., 2001, Chen et al., 2020). This quasi-steady approximation is
87 applicable for droplet growth where the supersaturation is typically less than 1% and the difference between the droplet
88 temperature and ambient air is negligible. For evaporation, where vapor deficits can occur over a wide range of relative
89 humidities, the approximation breaks down as the droplet temperature can deviate significantly from the ambient
90 environment (Srivastava and Coen, 1992; Roy et al., 2023).

91
92 Few studies in the cloud microphysics literature have carried out explicit numerical estimations and evolutions of
93 supercooled, evaporating cloud droplet temperatures and lifetimes for a wide range of environmental conditions. Roy
94 et al., (2023) provides a comprehensive review of past theoretical, numerical, or experimental studies of droplet
95 evaporation. Most of these studies examined the evaporation of raindrops for above 0°C temperatures (Kinzer and
96 Gunn, 1951; Watts 1971; Watts and Farhi, 1975), either assuming steady-state expressions (Beard and Pruppacher,
97 1971) or simplifying assumptions of linear dependence of saturation vapor density on temperature (Kinzer and Gunn,
98 1951; Watts 1971; Watts and Farhi, 1975). Srivastava and Coen (1992) assumed the heat storage term in the droplet
99 heat budget to be negligible, and investigated the evaporation of isolated, stationary hydrometeors by iteratively
100 solving the steady-state solutions, using saturation vapor pressure relations from Wexler (1976) to calculate the
101 saturation vapor density. Roy et al., (2023), by including the heat storage term and solving for time-dependent heat
102 and mass transfer between single, stationary cloud droplets evaporating in infinitely large, prescribed ambient
103 environments, demonstrated that the temperatures of the cloud droplets (initial radii between $30\text{-}50\ \mu\text{m}$) reach steady-

Deleted: ¶

105 state quite quickly (within <0.5 s). They considered a wide range of environmental conditions and found that
106 evaporating droplet temperatures can typically be 1-5 K colder than that of the environment, with values as low as
107 ~ 10 K for low relative humidity, and low-pressure conditions with near 0°C environments. Their steady-state droplet
108 temperatures agreed well with those of Srivastava and Coen (1992). They showed that the droplet temperature during
109 evaporation can be approximated by the thermodynamic wet-bulb temperature of the ambient environment. For most
110 subsaturated conditions, radiative cooling in cloud-top environments was found to play a negligible role in altering
111 evaporating droplet temperatures, except for larger droplets in environments close to saturation.

112
113 However, two main issues have not yet been accounted for in the aforementioned studies. Firstly, water droplets were
114 considered to have a uniform bulk droplet temperature, based on the assumption of infinite thermal heat conductivity
115 of water, thus ignoring the added complexity of simulating the internal thermal gradients within the droplet. (Kinzer
116 and Gunn, 1951; Watts, 1971; Srivastava and Coen, 1992, Roy et al., 2023). As several studies suggest that the droplet
117 surface plays a special role in nucleating ice and evaporation being a surface phenomenon, accurate modeling of the
118 evolution of droplet surface temperature and internal thermal gradients within the droplet volume is required to
119 correctly predict the ice nucleation rates. Secondly, to date, none of these studies considered the spatiotemporally
120 evolving effects of thermal and moisture feedback between the droplet and its immediate environment. The rationale
121 for justifying the usage of constant ambient conditions far away from the droplet was mostly based on studies where
122 ambient conditions were defined by prescribed temperature and moisture fields far away from a droplet (Sedunov,
123 1974; Eq. 7.7 of Rogers and Yau, 1989; Srivastava and Coen, 1992). A correction to the ambient conditions at a radius
124 similar to the mean distance between droplets (~ 1 mm) was shown to lead to minimal modifications for typical cloud
125 conditions (Fukuta, 1992). Thus, this assumption holds for droplets distributed homogeneously in space. Concerning
126 numerically simulating the growth and decay of a droplet population, Grabowski and Yang (2013) stated: “Cloud
127 droplets grow or evaporate because of the presence of moisture and temperature gradients in their immediate vicinity,
128 and these gradients are responsible for the molecular transport of moisture and energy between the droplet and its
129 immediate environment. One may argue that these gradients need to be resolved to represent the growth accurately.
130 Elementary considerations demonstrate that the moisture and temperature gradients in the droplet vicinity are
131 established rapidly [i.e., with a characteristic timescale of milliseconds or smaller (e.g., Vaillancourt et al. 2001, and
132 references therein)]; thus, the steady-state droplet growth equation is accurate enough. More importantly, the volume
133 affected by these gradients has a radius of approximately 10 to 20 droplet radii.... One can simply neglect molecular
134 transport processes in the immediate droplet vicinity and simulate droplet growth using the Maxwellian approach, that
135 is, by applying the supersaturation predicted by the mean (over the volume occupied by the droplet) temperature and
136 moisture fields...(see Vaillancourt et al. 2001, appendix).”

137
138 Here, we quantitatively revisit these arguments within the context of an evaporating supercooled cloud droplet. We
139 use high-resolution modeling to resolve the spatiotemporally evolving unsteady thermal and vapor density gradients
140 in the vicinity of the droplet as well as include internal heat transfer within the droplet, relaxing the assumption of
141 infinite thermal heat conductivity of water. Using an advanced numerical model, our framework employs the finite-

142 element method to solve the Navier-Stokes and continuity equations, coupled with heat and vapor diffusion, with
143 appropriate boundary conditions. The results from this study extend the findings from Roy et al. (2023) that an
144 evaporating droplet can exist at a temperature lower than that of the ambient environment, and that the temperature
145 deviation increases from the steady-state value under certain environmental conditions. This may lead to significant
146 enhancement in ice nucleation by increasing the predicted number concentrations of activated ice-nucleating particles
147 (INPs) either immersed within or externally contacting the supercooled droplet. The current study advances the
148 numerical approach presented in Roy et al. (2023) by including the impact of internal heat gradients within the droplet
149 and spatiotemporally varying heat and mass transfer between the droplet and its immediate environment. We also
150 provide droplet lifetime comparisons with estimates from Roy et al. (2023) and pure diffusion-limited evaporation
151 calculations. The implications of the evaporating supercooled cloud droplet temperatures and lifetimes on ice
152 nucleation at cloud boundaries are discussed.

153

154 **2 Numerical Methodology**

155 **2.1 Description of COMSOL**

156

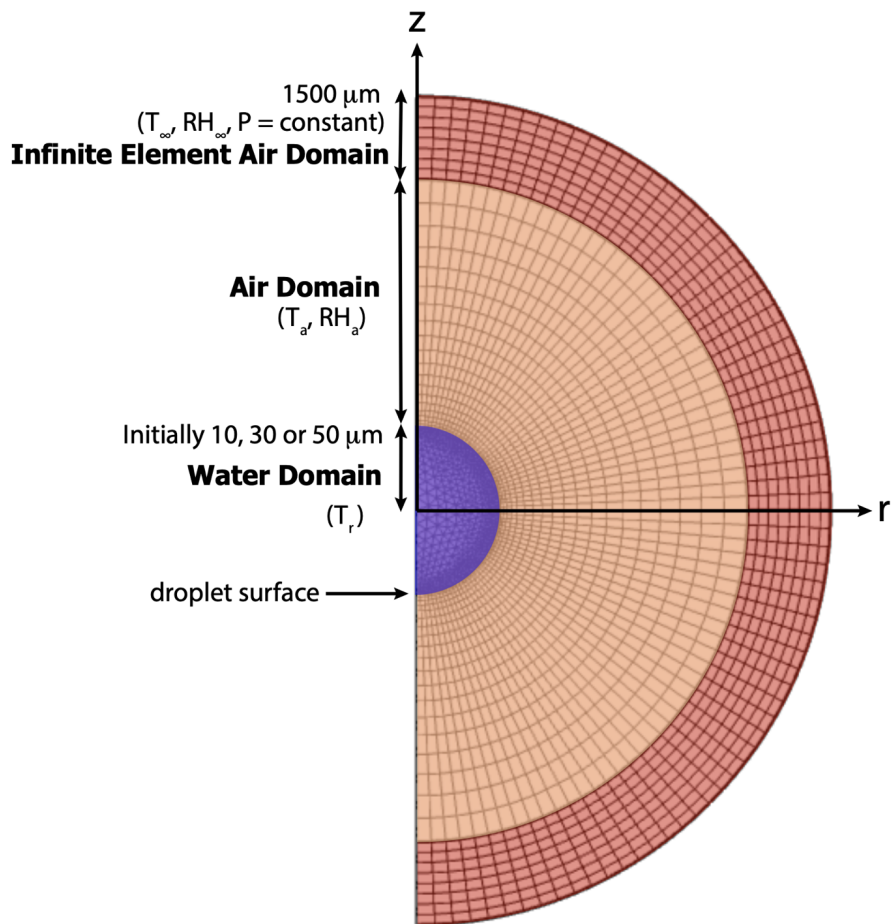
157 The simulation of the spatiotemporally varying droplet temperature and radius of an evaporating cloud droplet
158 embedded in a gaseous domain is difficult to solve analytically because of the moving and shrinking boundary at the
159 surface of the evaporating droplet. These kinds of moving boundary problems are known as Stefan problems. To
160 model this process, we have used an advanced numerical solver, COMSOL (Version 6.0), which employs a finite
161 element method to solve partial differential equations (PDEs). The COMSOL Multiphysics software simultaneously
162 uses spatial, material, and mesh coordinate systems described as the spatial frame, material frame, and mesh frame,
163 respectively. The spatial frame is a fixed, global, Euclidean coordinate system, which in 2D has spatial cartesian
164 coordinates (r, z) with the center of the droplet at $(r, z) = (0, 0)$ (Fig. 1). The material frame specifies the material
165 substance, in this case, water or air. The mesh frame is a coordinate system used internally by the finite element
166 method.

167

168 The Navier-Stokes and Fick's second law of diffusion equation, which follows from the continuity equation, along
169 with appropriate boundary conditions (see Sec. 3) are solved to conserve mass and momentum in the whole system.
170 The following physics interfaces in COMSOL were used to simulate droplet evaporation: (1) *Two-Phase Laminar*
171 *Fluid Flow*, which includes a moving mesh to track the shrinking water-air interface of the evaporating water droplet
172 and fluid-fluid interface that incorporates evaporative mass flux; (2) *Transport of Diluted Species* to track water vapor
173 diffusion through the air domain and predict the evaporation rate at the droplet surface; and (3) *Heat Transfer in Fluids*
174 which accounts for the non-isothermal flow within the computational domain, temperature-dependent saturation vapor
175 density at the droplet interface, and a boundary heat source to account for the latent heat of evaporation. The
176 computational domain also includes an infinite element air domain (COMSOL 2023b) to specify and maintain
177 boundary conditions far away from the droplet. The physics modules are coupled through non-isothermal flow

178 between heat transfer and fluid flow, and mass transport at the fluid–fluid interface between fluid flow and species
179 transport.

180
181 A non-uniform moving mesh was created by breaking down the computational domain into numerous fine elements
182 of variable sizes, using the Arbitrary Lagrangian-Eulerian technique (Yang et al., 2014) to accurately track the moving
183 air-water interface at the droplet surface. In the ALE technique, the spatial cartesian coordinate system (r, z) is fixed,
184 while the coordinates of the material (R, Z) and the mesh (R_m, Z_m) nodes are functions of time as the droplet evaporates.
185 However, the material and mesh node coordinates are always fixed in their respective frames. Initially, the spatial,
186 material and mesh frames are all identical. As the simulation starts, the material and mesh frames deform as the moving
187 boundary of the droplet shrinks during evaporation. After each time step, the deformed nodes are mapped to the spatial
188 frame, where calculations are performed. In this study, we have used triangular mesh elements (COMSOL 2023c)
189 within the droplet and quadrilateral mesh elements (COMSOL 2023d) for the rest of the domain as shown in Fig. 1.
190 The triangular mesh allows a higher resolution at the droplet surface, and both meshes adjust continually as the droplet
191 surface shrinks during evaporation. Finally, to simulate the water droplet evaporating in ambient air system, with
192 appropriate initial and boundary conditions, the discretized PDEs are numerically solved with adaptive time steps (\leq
193 0.01 s) to maintain numerical stability and obtain the solution (the temporal evolution of droplet temperature and
194 radius) for a range of conditions.



195
 196
 197
 198
 199
 200
 201
 202
 203

Figure 1: Schematic depicting the evaporating droplet, embedded in the air domain. The spatial frame (r, z) and the initial mesh frame (triangular elements within the droplet and quadrilateral elements outside the droplet) are shown (not to scale).

2.2 Justification for choice of environmental parameters in the simulations

204 Probing the evolution of the droplet and its immediate environment under a wide swath of conditions was
205 computationally too expensive, thus, certain choices regarding the parameter selection were made. The assumption
206 behind the computational set-up is that the supercooled droplet is suddenly introduced to a subsaturated environment
207 with ambient temperature, $T_\infty = 273.15$ K, 268.15 K, or 263.15 K, as might happen when the droplets are near cloud
208 boundaries such as those occurring in cloud-top generating cells. These temperatures are the ones where activation of
209 INPs is thought to be least effective. Calculations presented in Sec. 4 consider three different environments having
210 ambient relative humidity, $RH_\infty = 10, 40,$ and 70% , and two different ambient pressures, $P = 500,$ and 850 hPa, and
211 initial cloud droplet radii, $r_0,$ of $10, 30,$ and 50 μm . The pressure levels were chosen based on the occurrence of 273.15
212 K, 268.15 K, and 263.15 K in standard atmospheric profiles for tropical latitudes and middle latitudes under warm
213 and cool season conditions (Standard Atmosphere, 2021). Overall, 90 numerical experiments were performed using
214 various combinations of initial $RH_\infty, T_\infty, P,$ and r_0 to obtain a better understanding of the relationships between the
215 evolution of droplet temperatures and radii, and environmental variables. Of these, the results of 54 experiments are
216 reported in detail herein. The results of these experiments are later summarized in Figs. 3-10 and Tables 1-2. The
217 specific combinations of environmental parameters and initial droplet radii used in this study were also selected to
218 enable easy comparison with results from a previous study of droplet evaporation (Roy et al., 2023). Also, to be noted,
219 the effect of radiation in this study was neglected based on Roy et al. (2023), which demonstrated the negligible role
220 played by radiation in modifying evaporating droplet temperatures under most subsaturated conditions ($RH < 80\%$).

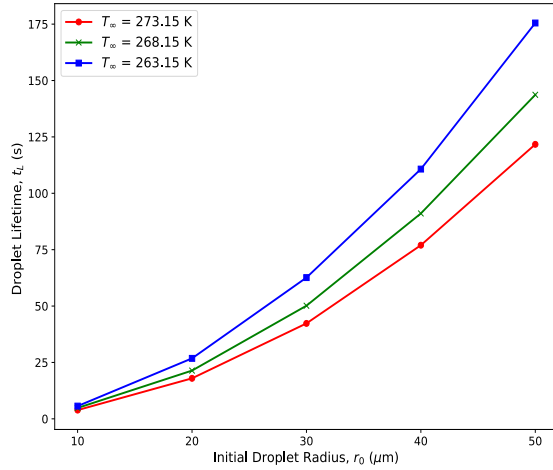
221

222 **2.3 Justification for choice of droplet lifetime cut-off**

223

224 For each experiment, the computational time rose exponentially to maintain numerical stability as the droplet radius
225 decreased during evaporation and the grid sizes needed to be smaller. To avoid exceptionally long computation time,
226 the cut-off radius for the simulations was set to be when the volume of the droplets decreased by 99.5% to reach 0.5%
227 of the initial droplet volume. For $r_0 = 10, 20, 30, 40, 50$ μm , the cutoff radii of the droplets are 1.71, 3.42, 5.13, 6.84,
228 and 8.55 μm , respectively. Note that due to the Raoult effect, for a solution droplet with a mass of dissolved and
229 ionized NaCl = 10^{-13} g, the reduction in the evaporation rate (dr/dt) from that of a pure water droplet is about 1% for
230 a 1 μm radius droplet and 4% for a 0.7 μm droplet. As all cut-off radii considered here are > 1 μm , the solute effect
231 can be neglected. From the Kelvin equation, the equilibrium vapor pressure over a curved surface of pure water
232 approaches the value of equilibrium vapor pressure over a flat surface of pure water for a radius > 0.01 μm . Thus,
233 curvature effects were also neglected. For simplicity, we will refer to the cutoff time as the *droplet lifetime*, although
234 the droplets will survive for a longer time before complete evaporation. The droplet lifetime increases with the initial
235 droplet radius, higher atmospheric pressure, and higher RH_∞ (Fig. 2).

236



237
 238 **Figure 2: Droplet lifetimes, t_L in seconds, for droplets with varying initial droplet radii, $r_0 = 10, 20, 30, 40$ and $50 \mu\text{m}$,**
 239 **evaporating in an initial ambient environment with three different ambient temperatures, $T_\infty = 273.15$ (0°C), 268.15 (-5°C)**
 240 **and 263.15 (-10°C) K, with relative humidity, $RH_\infty = 70\%$, with pressure, $P = 850$ hPa.**
 241

242 **2.4 Sensitivity to domain size**

243
 244 It was important to ensure that the spatiotemporally varying thermal and vapor density gradients in the ambient air in
 245 the vicinity of the evaporating droplet don't interfere with the constant ambient conditions (RH_∞ and T_∞) at the external
 246 boundary of the computational domain. Sensitivity tests with different air domain sizes of 10, 30, and 50 times the
 247 initial droplet radius were carried out to determine the droplet temperature and radial dependence on domain size. It
 248 was found that the evolution of droplet temperature and radius was not sensitive to domain sizes larger than 10 times
 249 the droplet radius considered. Based on the sensitivity analysis, the maximum size of the computational domain for
 250 all experiments was fixed at $1500 \mu\text{m}$, 30 times the largest droplet considered.

251 **3 Theory**

252 **3.1 Assumptions**

253
 254 The framework of the numerical model assumes that an isolated, stationary, spherical, pure water droplet is suspended
 255 within a 2D axisymmetric ambient air domain with constant ambient temperature ($\leq 0^\circ\text{C}$) and relative humidity
 256 ($<100\%$) at a sufficiently far distance away from the droplet that the droplet evaporation does not influence the far
 257 environment. The water droplet and air are considered to be Newtonian fluids, with the assumption that no internal
 258 circulation occurs within the droplet and that there is no ventilation, no radiative heat transfer, and negligible buoyancy
 259 effects due to gravity. This computational approach is an advanced form of the one described in Roy et al., (2023),
 260
 261

262 but also includes the effect of internal droplet heat transfer and spatiotemporal gradients in temperature and vapor
 263 density between the droplet and the environment (see discussion in Sec. 5).

264

265 3.2 Governing Equations

266

267 Based on the above assumptions, the following are the equations governing the system during droplet evaporation in
 268 the ambient air.

269

270 (1) Fluid flow: The *Laminar Flow* interface models the weakly compressible form of the Navier-Stokes equation,
 271 along with the continuity equation in the water and air domains,

272

$$273 \quad \rho \frac{\partial \mathbf{u}}{\partial t} + \rho(\mathbf{u} \cdot \nabla) \mathbf{u} = \nabla \cdot [-p\mathbf{I} + \boldsymbol{\tau}] + \mathbf{F} \quad (1)$$

$$274 \quad \boldsymbol{\tau} = \mu(\nabla \mathbf{u} + (\nabla \mathbf{u})^T) - \frac{2}{3}\mu(\nabla \cdot \mathbf{u})\mathbf{I} \quad (2)$$

$$275 \quad \frac{\partial \rho}{\partial t} + \nabla \cdot (\rho \mathbf{u}) = 0 \quad (3)$$

276

277

278 where t is time, ρ is the fluid density (kg/m^3), \mathbf{u} is the fluid velocity vector (m/s), p is pressure (Pa), \mathbf{I} is the identity
 279 tensor, $\boldsymbol{\tau}$ is the viscous stress tensor (Pa), \mathbf{F} is the external volume force vector (N/m^3), which is assumed to be
 280 negligible here, and μ is the fluid dynamic viscosity. For water below 273.15 K, the dynamic viscosity can be
 281 approximated as 1.79 mPa s. For air, COMSOL uses an empirical equation that produces values equivalent to

282 Sutherland's law (White, 2006), $\mu = \mu_0 \left(\frac{T}{T_0}\right)^{\frac{3}{2}} \left(\frac{T_0 + S_\mu}{T + S_\mu}\right)$ where $\mu_0 = 1.716 \times 10^{-5} \text{ N s m}^{-2}$, $T_0 = 273 \text{ K}$, and $S_\mu = 111 \text{ K}$
 283 for air. The empirical equation is given as:

$$284 \quad \mu = -8.38278 \times 10^{-7} + 8.35717342 \times 10^{-8}T - 7.69429583 \times 10^{-11}T^2 + 4.6437266 \times 10^{-14}T^3 -$$

$$285 \quad 1.06585607 \times 10^{-17}T^4 \quad (4)$$

286

287 (2) Heat Transport: The *Heat Transfer in Fluids* interface models heat transfer in all domains (air, water, infinite
 288 element domain) using the following version of the heat equation:

289

$$290 \quad \rho C_p \frac{\partial T}{\partial t} + \rho C_p \mathbf{u} \cdot \nabla T + \nabla \cdot \mathbf{q} = 0 \quad (5)$$

$$291 \quad \mathbf{q} = -k \nabla T \quad (6)$$

292

293 where ρ (kg/m^3) is the fluid density, C_p ($\text{J}/(\text{kg} \cdot \text{K})$) is the fluid heat capacity at constant pressure, T is the temperature,
 294 k ($\text{W}/(\text{m} \cdot \text{K})$) is the fluid thermal conductivity, \mathbf{u} (m/s) is the fluid velocity field from the *Laminar Flow* interface, \mathbf{q}
 295 (W/m^2) is the heat flux by conduction. We chose the value of k for supercooled water at $0.56 \text{ W m}^{-1} \text{ K}^{-1}$ based on Fig.
 296 3 of Biddle et al., (2013) where the thermal conductivity of supercooled water is very close to $0.56 \text{ W}/(\text{m} \cdot \text{K})$ for the

297 range of temperatures used in this study. Based on Beard and Pruppacher (1971), the thermal conductivity of air, given
 298 by $k_a = 0.004184[5.69 + 0.017(T - 273.15)]$ ($\text{W m}^{-1} \text{K}^{-1}$), has very weak dependence on temperature over the
 299 temperature range used in this study. For both $T = 273.15 \text{ K}$ and 253.15 K , the value of k_a is $0.02 \text{ W m}^{-1} \text{K}^{-1}$. Hence,
 300 we have used a constant value of $0.02 \text{ W m}^{-1} \text{K}^{-1}$.

301
 302 (3) Mass transport: The *Transport of Diluted Species* interface models water vapor transport through Fick's laws of
 303 diffusion, solving the mass conservation equation for vapor transfer in all domains except within the cloud droplet:

$$304 \quad \frac{\partial c}{\partial t} + \nabla \cdot \mathbf{J} = 0 \quad (7)$$

$$305 \quad \mathbf{J} = -D \nabla c \quad (8)$$

306
 307 where c is the concentration of water vapor (mol/m^3), D denotes the diffusion coefficient (m^2/s), and \mathbf{J} is the mass flux
 308 diffusive flux vector ($\text{mol}/(\text{m}^2 \cdot \text{s})$). D is calculated following Hall and Pruppacher (1976) and defined as follows: $D =$
 309 $0.0000211 \frac{P_0}{P} \left[\frac{T}{T_0} \right]^{1.94}$ ($\text{m}^2 \text{ s}^{-1}$) with reference pressure, $P_0 = 1013.25 \text{ hPa}$, reference temperature, $T_0 = 273.15 \text{ K}$,
 310 atmospheric temperature, T , and pressure, P . In this study, values of P are either fixed at 500 or 850 hPa to determine
 311 the effect of ambient air pressure on droplet evaporation. \mathbf{J} is obtained from the Laminar Flow interface through
 312 coupling between these interfaces.
 313

314 3.3 Initial conditions

316 The initial velocity components in the r , and z directions are assumed to be 0 m/s in both air and water domains. The
 317 initial fluid pressure is $p = P_{0,air}$ (Pa), specified either at 500 or 850 hPa in the air domain, and in the water domain, p
 318 $= P_{0,water} = \frac{2\sigma}{r_0}$ Pa, where surface tension, $\sigma = 70 \times 10^{-3} \text{ (N/m)}$. For the heat transfer module, all domains are assumed
 319 to be at a prescribed initial ambient temperature, T_0 , which is the same as that of a point at a far distance away from
 320 the droplet, T_∞ .

321 For the vapor transfer interface, except within the droplet, all domains are at an initial vapor concentration of $c_{0,air}$
 322 which is again assumed to be the same as that of the constant ambient concentration value far from the droplet, c_∞ ,
 323 calculated as follows:

$$324 \quad c_\infty = \frac{RH_\infty \times e_{sT_\infty}}{R_{univ} \times T_\infty} \text{ where, } RH_\infty \text{ is set at a constant ambient relative humidity far from the droplet, } R_{univ} = 8.3145$$

$$325 \quad (\text{J/mol/K}), T_\infty \text{ is in K. The saturation vapor pressure is calculated as, } e_{sT_\infty} = 610.94 * \exp\left(\frac{17.625 + T_\infty}{T_\infty + 243.04}\right) \text{ (in Pa, with}$$

326 T_∞ in $^\circ\text{C}$) following Alduchov and Eskridge (1996).

327
 328

329 **3.4 Model Constraints and Boundary Conditions**

330

331 1. Within the droplet and throughout the domain, the following conditions are applicable:

332
$$\mathbf{u} \cdot \mathbf{n} = 0 \quad (9)$$

333
$$[-p\mathbf{I} + \boldsymbol{\tau}] \cdot \mathbf{n} = 0 \quad (10)$$

334
$$\mathbf{q} \cdot \mathbf{n} = -k\nabla T \cdot \mathbf{n} = 0 \quad (11)$$

335
$$-D\nabla c \cdot \mathbf{n} = 0 \quad (12)$$

336 where \mathbf{n} is the normal to an outward-pointing vector from the center of the droplet. This constraint limits water
337 mass, water vapor and heat flow to the direction normal to the droplet surface.

338

339 2. At the fluid-fluid interface i.e., droplet-air boundary, the droplet surface is assumed to be at vapor saturation
340 throughout its lifetime. Hence, saturated vapor concentration at the shrinking droplet boundary, using the ideal gas

341 law, is given by, $c_{sat}(T_{sf}) = \frac{e_s(T_{sf})}{R_{univ} \times T_{sf}}$ where T_{sf} is the surface temperature, in K. The saturation vapor pressure $e_s(T_{sf})$

342 is estimated as $e_s(T_{sf}) = 610.94 * \exp\left(\frac{17.625 * T_{sf}}{T_{sf} + 243.04}\right)$ (in Pa, with T_{sf} in °C) again following Alduchov and Eskridge
343 (1996).

344

345 The local evaporative mass flux at the interface is given by diffusion of water vapor across the water-air interface, M_j
346 (kg/ m² s)

347
$$\mathbf{M}_j = M_w \mathbf{n} \cdot (-D\nabla c) \quad (13)$$

348

349 where the molecular weight of water, $M_w = 0.018$ (kg/mol). Although the temperature is continuous across the droplet-
350 air boundary, there is a discontinuity in heat flux across the interface due to the evaporation of water. Thus, the latent
351 heat of evaporation L , defined as $L = [2501 - 2.44T_r]$ kJ kg⁻¹ with droplet surface temperature, T_r in °C, is
352 incorporated as a boundary heat sink as $-M_j L$ (W/m²).

353

354 The mass balance at the water-vapor boundary at the droplet surface, and the velocity of the moving mesh \mathbf{u}_{mesh} , at
355 the shrinking water-air interface, are expressed by the following equations, based on Scardovelli and Zaleski, (1999):

356

357
$$\mathbf{u}_w = \mathbf{u}_v + M_j \left(\frac{1}{\rho_w} - \frac{1}{\rho_v} \right) \mathbf{n} \quad (14)$$

358

359
$$\mathbf{u}_{mesh} = (\mathbf{u}_w \cdot \mathbf{n} - \frac{M_j}{\rho_w}) \mathbf{n} \quad (15)$$

360

361 where the subscripts w and v represent water and vapor respectively.

362

363 The stresses are balanced at the water-vapor interface by the following conditions, based on Yang et al., (2014):

364
365
$$\mathbf{n} \cdot (\mathbf{S}_w - \mathbf{S}_v) = \sigma(\nabla_\sigma \cdot \mathbf{n})\mathbf{n} - \nabla_\sigma \sigma \quad (16)$$

366
$$\mathbf{S} = [-p\mathbf{I} + \boldsymbol{\tau}] \quad (17)$$

367

368 where \mathbf{S} is the total stress tensor and ∇_σ is the surface gradient operator defined by

369
370
$$\nabla_\sigma = (\mathbf{I} - \mathbf{n} \cdot \mathbf{n}^T)\nabla \quad (18)$$

371

372 In the normal direction of the boundary, the force is balanced by,

373
374
$$\mathbf{n} \cdot (\mathbf{S}_w - \mathbf{S}_v) = \frac{\sigma}{r_c} \cdot \mathbf{n} \quad (19)$$

375

376 where r_c is the curvature radius.

377

378 3. The external air domain boundary is open with the following condition:

379
$$[-p\mathbf{I} + \boldsymbol{\tau}]\mathbf{n} = -f_0\mathbf{n}, \quad (20)$$

380 where normal stress, $f_0 = 0 \text{ N/m}^2$.

381

382 4. The infinite element domain consists of air and is considered to be an ideal gas. The temperature, relative humidity,
383 and concentration far from the droplet i.e., at the inner boundary of the infinite element domain, are fixed at T_∞ and
384 c_∞ , respectively.

385

386 3.5 Coupling between the COMSOL interfaces

387

388 To numerically model the evaporating droplet embedded in the air domain, intercoupling between the three physics
389 interfaces - laminar two-phase flow (formulated within the Arbitrary Lagrangian-Eulerian framework), the heat
390 transfer in fluids, and the transport of diluted species within the air medium are established through the following
391 mechanisms: (i) the local evaporative mass flux at the droplet-air interface, which is related to the mesh velocity for
392 the laminar flow, is estimated by the diffusion of water vapor in the air domain; (ii) saturated vapor concentration at
393 the droplet-air interface, which serves as a boundary condition for the vapor diffusion, is calculated using the local
394 temperature at the droplet interface; and (iii) the evaporative heat flux at the droplet-air interface acts as a heat sink
395 boundary condition for the heat transfer in fluids module.

396

397 4 Results

398

399 Since evaporation is a surface phenomenon, with the evaporative cooling at the droplet surface acting as a heat sink,
400 the temperature of the evaporating droplet surface should be lower than the center of the droplet. In all simulations,

401 the center to surface temperature gradient within the droplet forms almost instantaneously as evaporative cooling at
402 the droplet surface occurs extremely fast. The time required for the droplet to reach internal thermal equilibrium
403 depended slightly on the initial size of the droplet and the ambient RH_∞ , with larger droplets and drier environments
404 leading to more time required by the droplets to reach equilibrium. However, generally, for typical cloud droplet sizes
405 and environmental conditions considered here ($r_0 = 10, 30, 50 \mu\text{m}$), the internal thermal gradients dissipate and the
406 temperatures throughout the droplets become uniform in $\leq 0.3 \text{ s}$, consistent with Fick's laws of diffusion with a
407 diffusive timescale of r^2/D , where r is the length scale and D is the thermal diffusivity of water. For this study, we
408 have simulated internal droplet heat transfer for the entirety of the droplet lifetime and will be reporting the average
409 droplet temperatures as "droplet temperatures" in the results, unless noted otherwise.

410
411
412
413

4.1 Droplet Thermal and Radial Evolution: Influence of Initial Droplet Size and Environmental Factors

414 Figures 3 and 4 depict the early evolution of the droplet average temperatures and radii ($r_0 = 10, 30$ and $50 \mu\text{m}$) for
415 the first few seconds of their lifetimes (as defined in Sec. 2c), for different environments with constant ambient
416 conditions (T_∞ , RH_∞ , and P) far from the droplet. Tables 1 and 2 provide the final temperature values and total lifetimes
417 of the droplets. Figures 3 and 4 also state the droplet temperatures at the end of their lifetimes (T_L) and the total
418 lifetimes of the droplets (t_L). For all numerical experiments, the evaporating droplet temperature decreases sharply,
419 within $< 0.5 \text{ s}$, to a certain temperature defined here as the transition point, T_i , where the slope of the curve changes.
420 After reaching T_i , the decrease in droplet temperature is relatively more gradual as can be seen from Figs. 3 and 4. For
421 example, in Fig. 3(c), for $P = 500 \text{ hPa}$, $T_\infty = 268.15 \text{ K}$ (-5°C), $RH_\infty = 10\%$, a droplet with $r_0 = 10 \mu\text{m}$, takes about 0.03
422 s to reach T_i at 260.98 K (a decrease of 7.17 K from initial temperature). In contrast, a $30 \mu\text{m}$ droplet takes about 0.12
423 s to reach T_i at 260.85 K (a decrease of 7.3 K from initial temperature), and a $50 \mu\text{m}$ droplet takes about 0.33 s to
424 reach T_i . Finally, the $10 \mu\text{m}$ droplet reaches the end of its lifetime in 1.05 s i.e. $t_L = 1.05 \text{ s}$ with temperature, $T_L =$
425 244.12 K after reaching T_i , while for the $30 \mu\text{m}$ droplet, $t_L = 11.4 \text{ s}$ with $T_L = 244.31 \text{ K}$, and $t_L = 32.76 \text{ s}$ for the $50 \mu\text{m}$
426 droplet with $T_L = 244.29 \text{ K}$ after reaching T_i .

427

428 The evaporation process in these experiments starts in a condition that is far from equilibrium. The coupled air- droplet
429 system attempts to evolve towards a steady-state where the thermal energy towards the droplet compensates for
430 evaporative cooling at the droplet surface. In this process, the droplet initially rapidly cools to the thermodynamic
431 wet-bulb temperature of the initial environment similar to what has been shown in Roy et al., (2023). However, under
432 low relative humidity conditions, the thermal and vapor diffusion are not yet near equilibrium. As the system attempts
433 to achieve a steady-state, the imbalance in the heat fluxes associated with vapor and thermal diffusion in the immediate
434 vicinity of the drop leads to a gradual reduction in the wet-bulb temperature of the immediate droplet environment
435 leading to a continued slow decrease in the droplet temperature as the droplet continues to evaporate.

436

437 In general, we can see that a higher ambient T_∞ , and lower RH_∞ and P leads to a larger reduction in droplet temperature
438 from its initial temperature. Therefore, drier, relatively warmer (closer to 0°C), and lower-pressure environments lead

439 to the strongest evaporative cooling of the droplets. Also, due to evaporative cooling, the droplets survive longer as
440 compared to the pure diffusion-limited evaporation approach where the decreases in evaporating droplet temperature
441 have not been considered (see Sec. 5). However, drier, relatively warmer (close to 0°C), and lower-pressure
442 environments lead to smaller droplet lifetimes as compared to more humid environments, with lower ambient
443 temperatures and higher pressures.

444

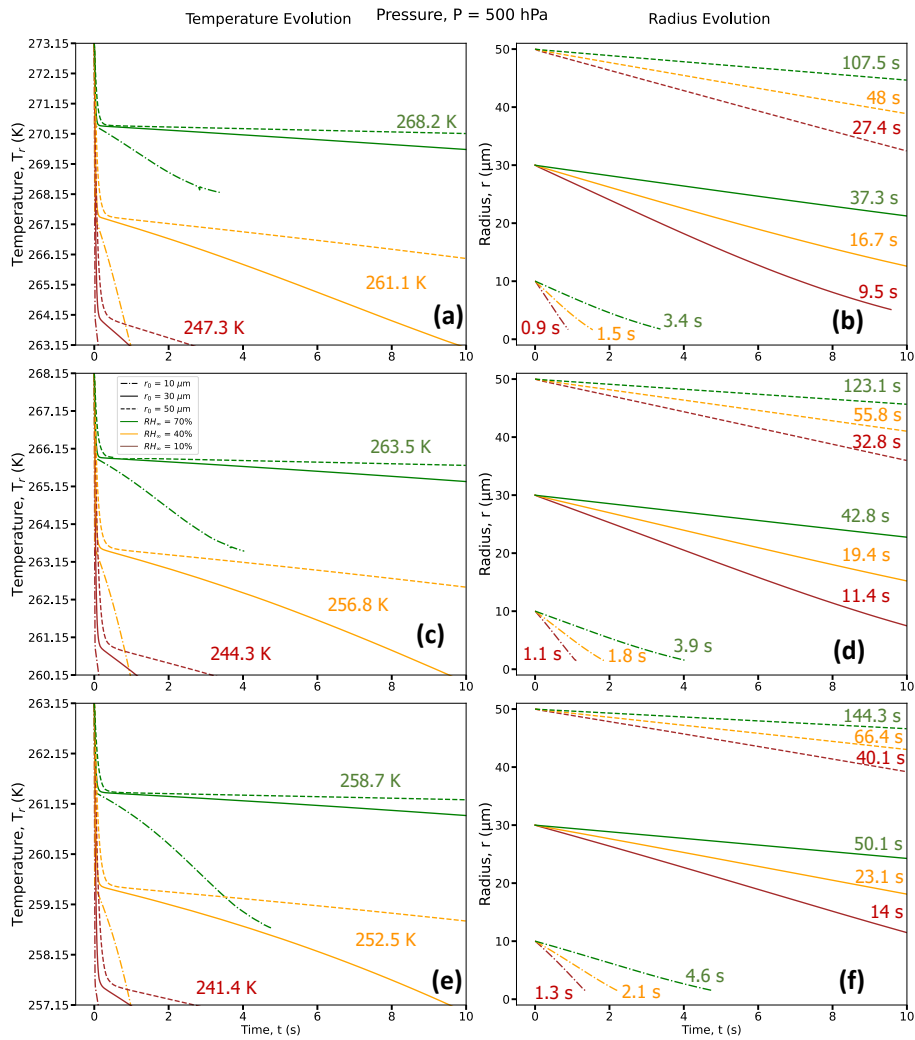
445 **4.2 Environmental Evolution: Evolution of Temperature, Relative Humidity, and Wet-Bulb Temperature in** 446 **the air domain near the droplet**

447

448 Figures. 5-7 (a, d) show radial cross sections of the computational domain, starting from the center of the droplet at
449 $(r, z) = (0, 0)$, along the r axis to the edge of the domain at $r = 1500 \mu\text{m}$, while Figs. 5-7 (b, e) expand the dashed box
450 regions of Figs. 5-7 (a, d), and Figs. 5-7 (c, f) further expand the dashed box regions of Figs. 5-7 (b, e). All panels
451 show the spatiotemporal evolution of temperature (Fig. 5), relative humidity (Fig. 6), thermodynamic wet-bulb
452 temperature (Fig. 7), and droplet radius for a droplet with initial radius, $r_0 = 50 \mu\text{m}$, introduced to an initial environment
453 with pressure, $P = 500 \text{ hPa}$, ambient temperature, $T_\infty = 268.15 \text{ K}$ (-5°C), with two different relative humidities, RH_∞
454 = 10% and 70%. The evolution of temperature within the droplet is left of the dashed black line, which denotes the
455 droplet radius.

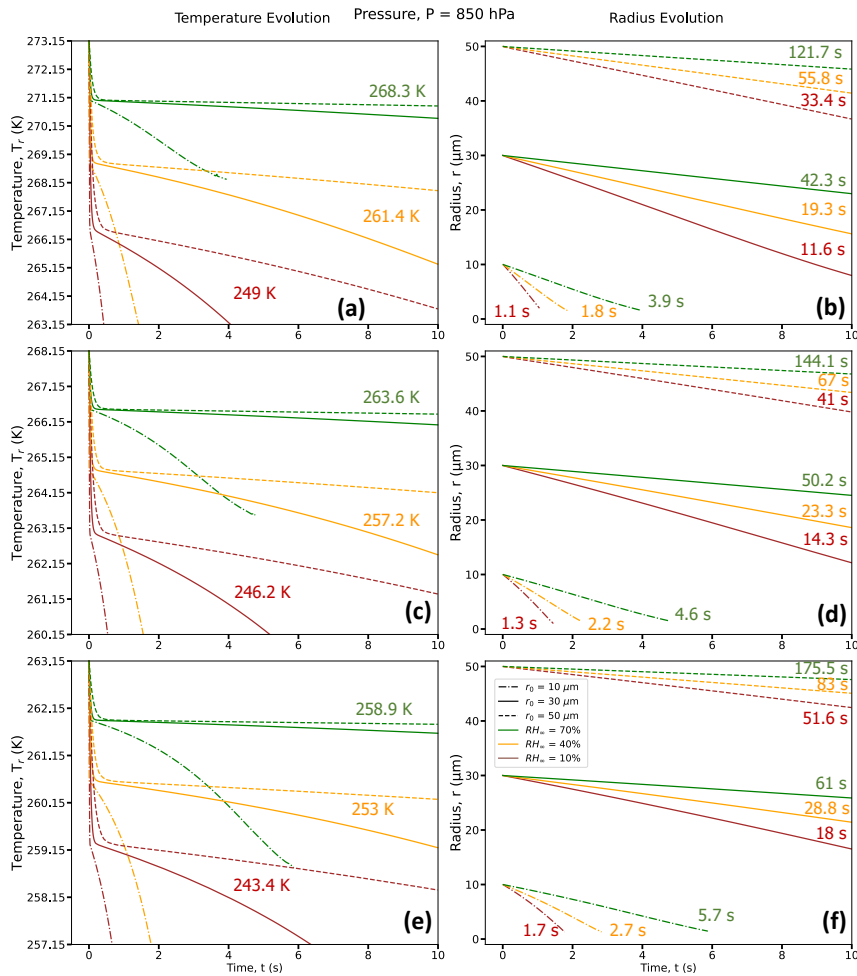
456

457 As the droplet evaporates in the subsaturated domain, evaporative cooling occurs at the droplet surface, leading to
458 heat transfer both from within the warmer droplet and the surrounding air to balance the cooling at the droplet surface.
459 Since the droplet has no constant internal heat source, the internal thermal gradients dissipate quite fast (within 0.3 s)
460 and the average droplet temperatures continue to decrease as the droplet evaporates. Due to heat exchange between
461 the droplet surface and the ambient air in its vicinity, transient thermal gradients in the ambient air develop and lead
462 to a decrease in the air temperature near the droplet. As the droplet shrinks in size along with cooling further, the
463 colder envelope of air surrounding the droplet shrinks as well and the ambient air far from the droplet, at a constant
464 temperature, acts as a heat source and supplies heat to the rest of the domain to attempt to equilibrate the air
465 temperature. Comparing Fig. 5 (a) and (d), at the lower RH_∞ , the magnitude of evaporative cooling is much higher.
466 For example, the average temperature of the $50 \mu\text{m}$ droplet decreases by $\sim 10 \text{ K}$ in 9 s when $RH_\infty = 10\%$, while the
467 decrease is $\sim 5 \text{ K}$ in 120 s, when $RH_\infty = 70\%$.



468
469

470 **Figure 3:** Droplet temperature evolution (left column) and radius evolution (right column) for three different RH_{∞} ($RH_{\infty} =$
471 10% (brown curves), 40% (orange curves) and 70% (green curves)), three different r_0 ($r_0 = 10 \mu\text{m}$ (dot-dashed lines), 30
472 μm (solid lines) and $50 \mu\text{m}$ (dashed lines)), with three different $T_{\infty} = 273.15 \text{ K}$ (0°C) (a, b), 268.15 K (-5°C) (c, d) and 263.15
473 K (-10°C) (e, f), for $P = 500 \text{ hPa}$. For each RH_{∞} , the average droplet temperature at the end of the lifetimes of the three
474 droplets with different r_0 (T_L , in K) is given in (a,c,e) and the time taken to reach the end of its lifetime (t_L , in s) is given in
475 (b, d, f). Exact values of final temperature for each r_0 are given in Table 1.

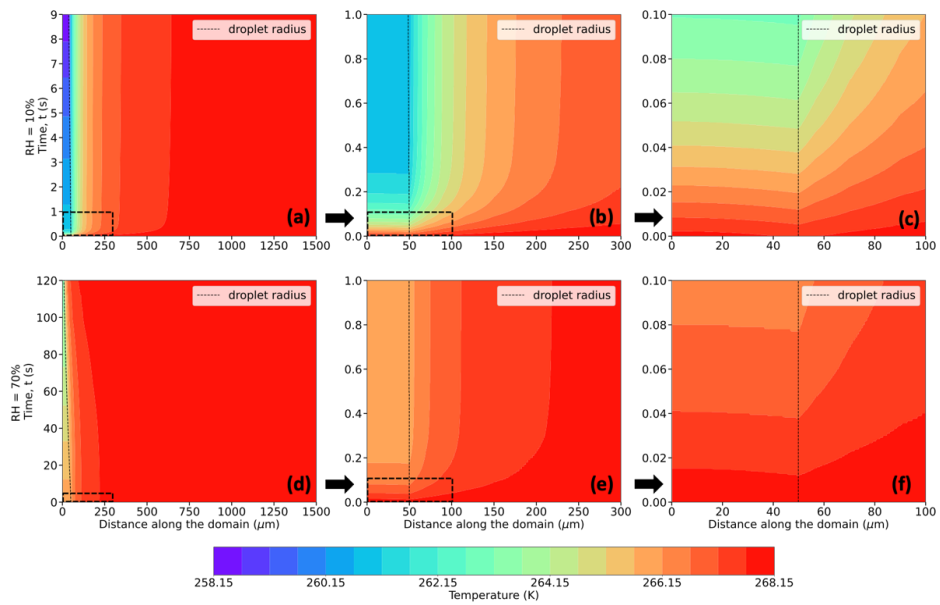


476

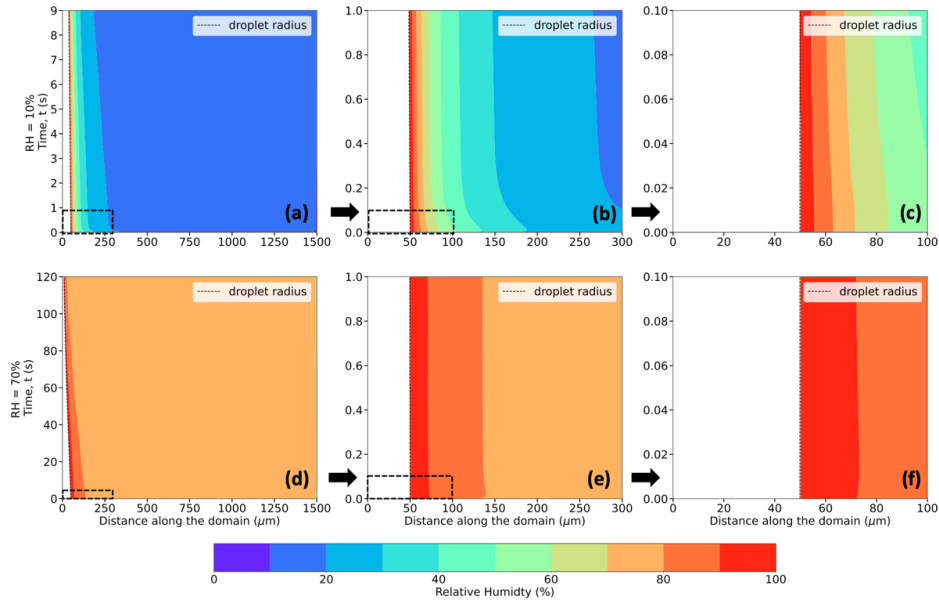
477 **Figure 4: Same as Fig. 3 but for $P = 850$ hPa.**

478

479 In these simulations, the air in contact with the droplet surface is saturated with respect to water, i.e., $RH = 100\%$ (Fig.
 480 6, a-f), consistent with assumptions of isolated, stationary evaporating droplets (Kinzer and Gunn, 1951; Srivastava
 481 and Coen, 1992). As the water vapor from the evaporating droplet surface diffuses into the surrounding environment,
 482 with an initial RH (same as RH_∞) of say 10%, vapor density gradients, similar to the thermal gradients, appear and
 483 impact the immediate environment of the droplet. These spatiotemporally varying thermal and vapor density gradients
 484 play an important role in affecting the droplet temperatures, evaporation rates, and in turn, droplet lifetimes.



485
 486 **Figure 5: Evolution of temperature (in K, shaded contours), and droplet radius (in μm, dashed black trace) for a 50 μm**
 487 **droplet, immersed in an environment with $T_{\infty} = 268.15$ K (-5°C), $P = 500$ hPa, and $RH_{\infty} = 10\%$ (top row) and 70% (bottom**
 488 **rows). Bottom left corner of each plot refers to the center of the droplet at $(r, z) = (0, 0)$. Distance along the domain refers**
 489 **to the radial distance from the center of the droplet. Figures denoted as (b) and (e), and (c) and (f) present zoomed-in plot**
 490 **areas marked by the dashed boxes in (a) and (d), and (b) and (e), respectively.**



492

493 **Figure 6: Same as Figure 5, but for Relative Humidity (in %, shaded contours), instead of Temperature.**

494

495 Roy et al. (2023) has shown that an evaporating cloud droplet temperature can be well-approximated by the
 496 thermodynamic wet-bulb temperature of the environment, especially at higher relative humidities and pressures, and
 497 lower ambient temperatures. Following the iterative procedure used in Roy et al. (2023) to calculate the
 498 thermodynamic wet-bulb temperature (T_{WB}), Fig. 7 (a-f) depicts the evolution of T_{WB} of the surrounding environment.
 499 Unlike previous studies (Srivastava and Coen, 1992; Roy et al., 2023), the ambient environment in this study is not
 500 assumed to be spatiotemporally invariant. Hence, as the thermal and vapor density gradients evolve in the ambient air,
 501 the T_{WB} of the environment evolves as well, depending on the temperature, relative humidity, and pressure, with the
 502 droplet surface temperature the same as that of the T_{WB} of its immediate environment at all times. Of interest, the
 503 droplet temperature decreases very quickly to T_i within < 0.5 s (Figs. 3 and 4), which agrees very well with the initial
 504 T_{WB} of the surrounding environment and the constant value of the thermodynamic wet bulb temperature far from the
 505 droplet ($T_{WB\infty}$). For example, in Fig. 7 (a-c), $T_{\infty} = 268.15$ K, $P = 500$ hPa, $RH_{\infty} = 10\%$, $T_{WB\infty} = 261.64$ K, and in Fig. 7
 506 (d-f), for $RH_{\infty} = 70\%$, $T_{WB\infty} = 266.13$ K. Fig. 7 shows the two phases of the evolution of T_{WB} of the immediate
 507 environment for two RH_{∞} environments – initially, there is a very fast decrease of the air temperature at the droplet
 508 surface to $T_{WB\infty}$ typically within < 0.3 s, and then a more gradual decrease of T_{WB} at the droplet surface as the thermal
 509 and vapor density gradients in the ambient air become relatively steadier and more established for a period of time,
 510 and as their spheres of influence start shrinking as the droplet starts getting smaller in size.

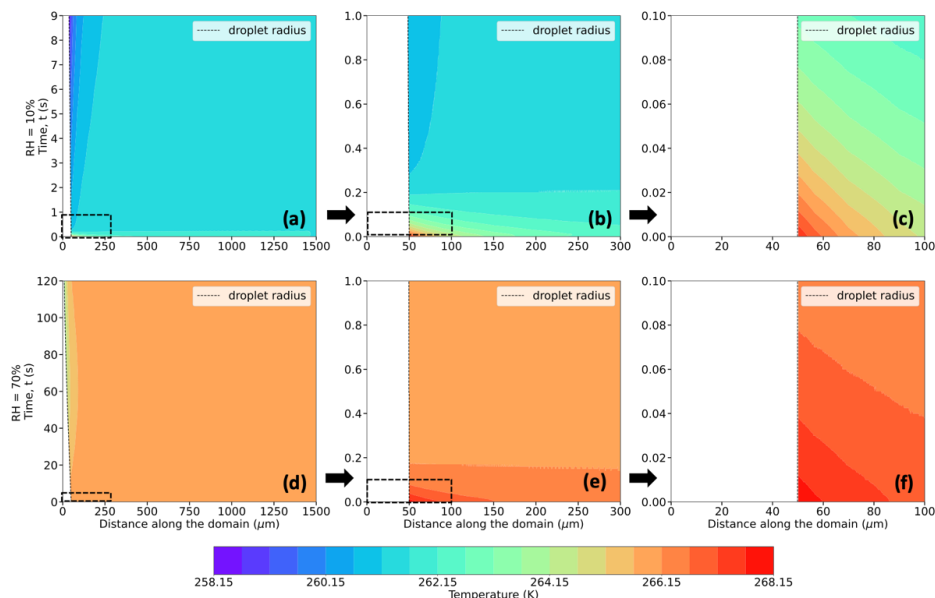


Figure 7: Same as Figure 5, but for thermodynamic wet-bulb temperature (in K, shaded contours).

4.3 Influence of initial droplet size and ambient environmental factors on the thermal evolution of the droplet and its surrounding environment

The overall results spanning the parameter space of the simulations are summarized in Tables 1-2 for the 54 numerical experiments using various combinations of ambient conditions (RH_{∞} , T_{∞} , and pressure, P , and r_0) specified at a distance far away from the droplet.

4.3.1 Effect of Ambient Relative Humidity, RH_{∞}

The decrease in droplet temperature is larger when the RH_{∞} is lower due to higher evaporation rates and stronger evaporative cooling under drier conditions. For instance, as shown in Table 1 and Fig. 8 (a, b, c), 30 μm droplets reach ~ 247.3 K (a decrease of 25.8 K from the initial temperature of 273.15 K) for $RH_{\infty} = 10\%$, ~ 261.1 K (a decrease of 12.1 K) for $RH_{\infty} = 40\%$ and ~ 268.2 K (a decrease of ~ 5 K) for $RH_{\infty} = 70\%$. The droplet lifetimes vary depending on RH_{∞} , with lifetimes increasing with an increase in humidity. For example, the droplet lifetimes for the 30 μm droplet are ~ 9.5 s, 16.7 s, and 37.3 s for environments with $RH_{\infty} = 10\%$, 40% and 70%, respectively (Table 2). The decrease in droplet temperature and increase in droplet lifetime show similar dependence with increasing RH_{∞} for 10 and 50 μm droplets as well.

531 **4.3.2 Effect of Initial Droplet Size, r_0**

532

533 From Figs. 8-10, for a given initial environmental condition (RH_∞ and T_∞), the droplet temperatures at the end of their
534 lifetimes are independent of the initial droplet sizes. For example, from Table 1 and Fig. 9 (a-i) at $P = 500$ hPa, 10,
535 30 and 50 μm droplets reach ~ 244 K (a decrease of ~ 24 K from the initial temperature of 268.15 K) for $RH_\infty = 10\%$,
536 ~ 256.8 K for $RH_\infty = 40\%$, and ~ 263.5 K for $RH_\infty = 70\%$. On the other hand, the droplet lifetime strongly depends on
537 the initial droplet size, as the larger droplets take more time to evaporate as compared to the smaller ones. For
538 environments with $RH_\infty = 10\%$, 40% and 70%, the droplet lifetimes for the 10 μm droplet are ~ 1.1 s, 1.8 s, and 3.9 s,
539 while for the 30 μm droplet are ~ 11.4 s, 19.4 s, and 42.8 s, and for the 50 μm droplet are ~ 32.8 s, 55.8 s, and 123.1
540 s, respectively (Table 2). For a higher pressure of $P = 850$ hPa (Table 1), at the same T_∞ , irrespective of r_0 , the decrease
541 in droplet temperatures is slightly smaller as compared to $P = 500$ hPa, with values of 22 K, 11 K, and 4.6 K. The
542 radial dependence of the thermal gradients in the ambient air also depends on the initial droplet size, decreasing with
543 a decrease in r_0 .

544

545 **4.3.3 Effect of Ambient Temperature, T_∞**

546

547 To determine the effect of a lower ambient temperature on droplet temperatures and lifetimes, Figs. 9 and 10
548 demonstrate similar plots as shown in Fig. 8, but for $T_\infty = 268.15$ K (-5°C) and 263.15 K (-10°C), respectively. The
549 decrease in droplet temperatures and increase in droplet lifetimes depict similar relationships with RH_∞ and r_0 .
550 Droplets, irrespective of their initial size, cool to a lower temperature depending on the ambient RH_∞ , with the
551 magnitude of the cooling being inversely proportional to the subsaturation of the ambient environment. For instance,
552 for 10, 30 and 50 μm droplets, from an initial temperature of 268.15 K, the droplet temperatures approximately
553 decrease by 24 K, 11.4 K, and 4.7 K, for environments with $RH_\infty = 10\%$, 40%, and 70%, respectively (Table 1). The
554 droplet lifetimes for the 10 μm droplet are ~ 1.1 s, 1.8 s, and 3.9 s, while for the 30 μm droplet are ~ 11.4 s, 19.4 s,
555 and 42.8 s, and for the 50 μm droplet are ~ 32.8 s, 55.8 s, and 123.1 s, for $RH_\infty = 10\%$, 40% and 70%, respectively
556 (Table 2). Comparing these values with those of $T_\infty = 273.15$ K (0°C), it can be noted that a lower ambient temperature
557 leads to a smaller decrease in droplet temperatures and a slight increase in droplet lifetimes in a spatiotemporally
558 evolving environment, for the same RH_∞ , r_0 and P . Fig. 10 and Table 1 depict that for $T_\infty = 263.15$ K (-10°C), the
559 reduction in droplet temperatures is slightly smaller, ~ 21.8 K, 10.7 K, and 4.5 K for environments with $RH_\infty = 10\%$,
560 40%, and 70%, respectively, and droplet lifetimes are longer relative to the higher ambient temperatures of 273.15 K
561 and 268.15 K (Table 2). This is because at a lower ambient temperature, the vapor diffusivity into the ambient air is
562 lower, leading to a weaker evaporation rate with slightly reduced cooling, and extended droplet lifetime, relative to
563 those in an environment with a higher ambient temperature.

564

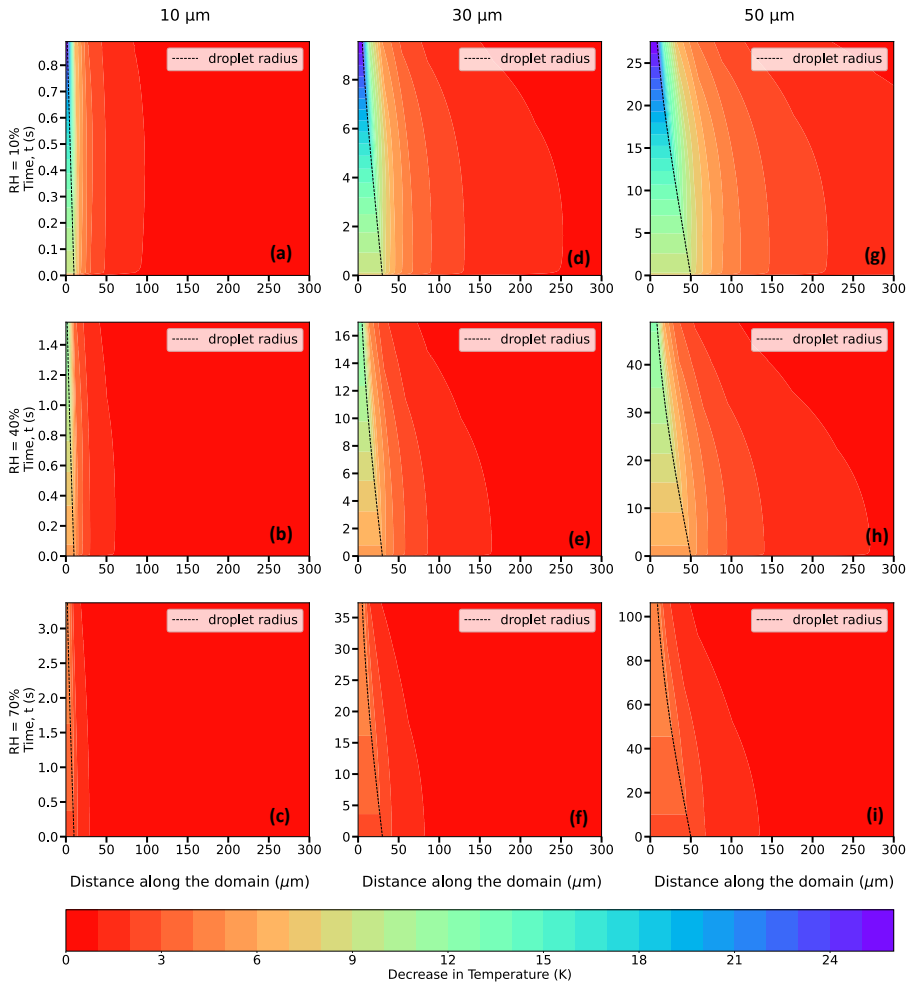
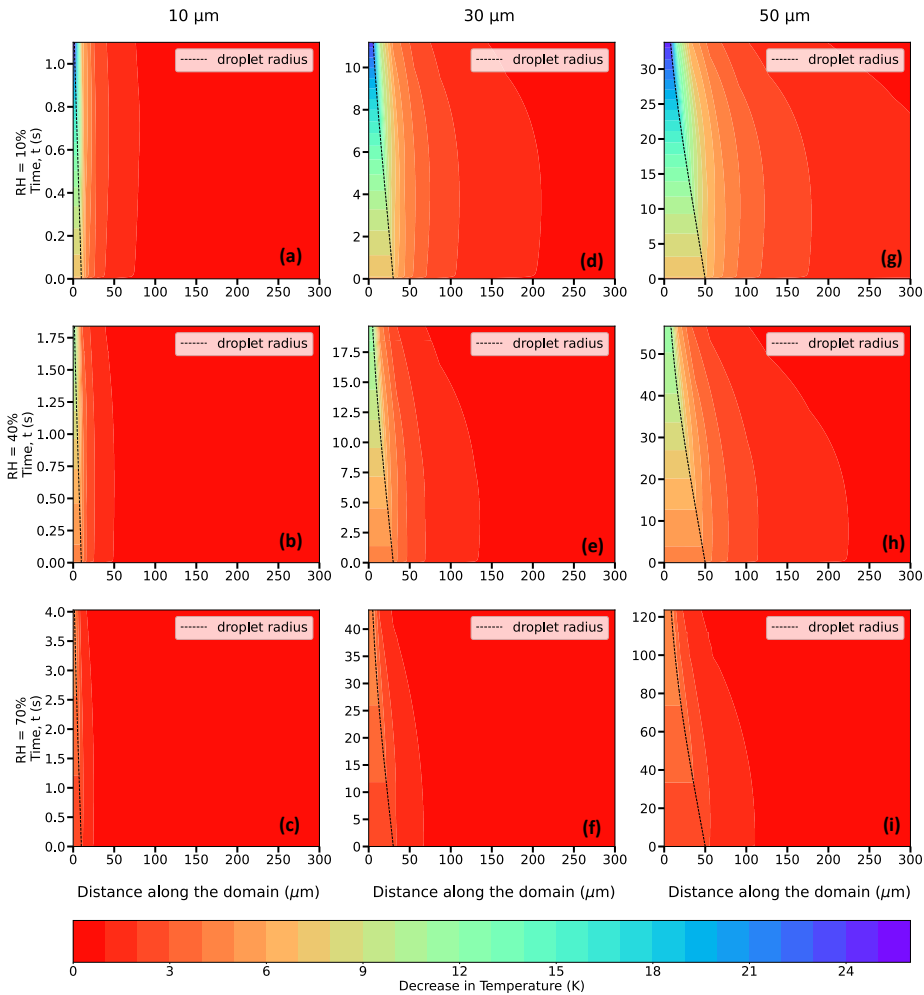


Figure 8: Evolution of the decrease in temperature (in K, shaded contours) from the initial temperature of the domain = 273.15 K (0°C), and of the droplet radius (in μm, dashed black trace) for 10 (a,b,c), 30 (d,e,f), and 50 (g,h,i) μm droplets, immersed in an environment with $T_{\infty} = 273.15$ K (0°C), $P = 500$ hPa, and $RH_{\infty} = 10\%$, 40% and 70% .

565
566
567
568
569
570
571
572
573
574
575
576

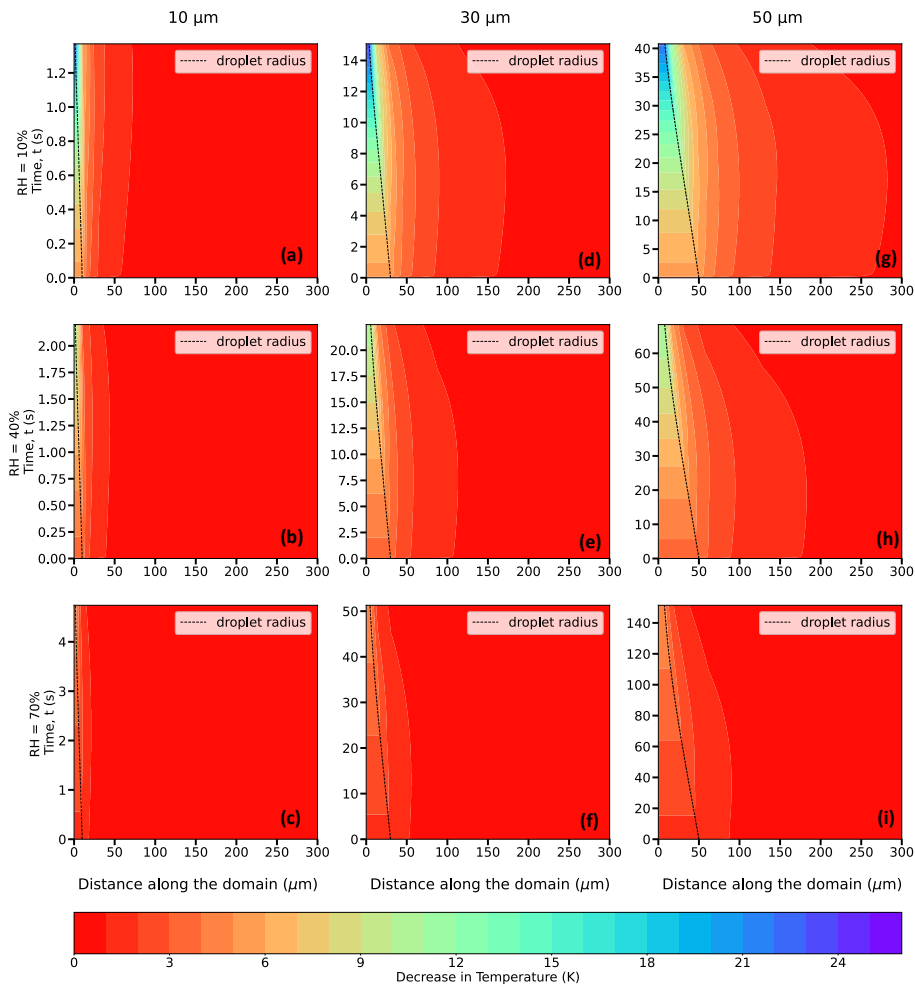
T_{∞} (K)	r_0 (μm)	RH_{∞} (%)	$P = 500 \text{ hPa}$					$P = 850 \text{ hPa}$				
			$T_{WB\infty}$ (K)	T_{RRD} (K)	T_i (K)	T_L (K)	$T_{\infty} - T_L$ (K)	$T_{WB\infty}$ (K)	T_{RRD} (K)	T_i (K)	T_L (K)	$T_{\infty} - T_L$ (K)
273.15 (0°C)	10	10	264.94	264.06	264.15	247.15	26	267.20	266.49	266.35	249.03	24.12
		40	267.95	267.41	267.35	261.09	12.06	269.30	268.85	268.95	261.40	11.75
		70	270.67	270.43	270.35	268.21	4.94	271.28	271.07	271.10	268.29	4.86
	30	10	264.94	264.06	264.15	247.33	25.82	267.20	266.49	266.37	249.01	24.14
		40	267.95	267.41	267.35	261.08	12.07	269.30	268.85	268.95	261.43	11.72
		70	270.67	270.43	270.45	268.20	4.95	271.28	271.07	271.15	268.26	4.89
	50	10	264.94	264.06	264.15	247.31	25.84	267.20	266.49	266.37	249.04	24.11
		40	267.95	267.41	267.36	261.09	12.06	269.30	268.85	268.95	261.45	11.7
		70	270.67	270.43	270.45	268.20	4.95	271.28	271.07	271.15	268.29	4.86
268.15 (-5°C)	10	10	261.64	260.90	260.98	244.12	24.03	263.57	263.01	263.15	246.32	21.83
		40	263.96	263.50	263.48	256.77	11.38	265.16	264.79	264.82	257.17	10.98
		70	266.13	265.91	265.9	263.47	4.68	266.68	266.51	266.65	263.57	4.58
	30	10	261.64	260.90	260.85	244.31	23.84	263.57	263.01	263.06	246.18	21.97
		40	263.96	263.50	263.46	256.76	11.39	265.16	264.79	264.69	257.18	10.97
		70	266.13	265.91	265.92	263.47	4.68	266.68	266.51	266.56	263.58	4.57
	50	10	261.64	260.90	260.85	244.29	23.86	263.57	263.01	263.06	246.21	21.94
		40	263.96	263.50	263.47	256.76	11.39	265.16	264.79	264.72	257.16	10.99
		70	266.13	265.91	265.92	263.46	4.69	266.68	266.51	266.56	263.56	4.59
263.15 (-10°C)	10	10	258.14	257.55	257.53	241.38	21.77	259.73	259.28	259.28	243.49	19.66
		40	259.89	259.51	259.65	252.46	10.69	260.90	260.60	260.65	252.97	10.18
		70	261.56	261.38	261.4	258.73	4.42	262.04	261.90	261.90	258.88	4.27
	30	10	258.14	257.55	257.62	241.36	21.79	259.73	259.28	259.28	243.27	19.88
		40	259.89	259.51	259.56	252.47	10.68	260.90	260.60	260.54	252.99	10.16
		70	261.56	261.38	261.39	258.73	4.42	262.04	261.90	261.91	258.88	4.27
	50	10	258.14	257.55	257.62	241.37	21.78	259.73	259.28	259.28	243.48	19.67
		40	259.89	259.51	259.56	252.47	10.68	260.90	260.60	260.56	252.99	10.16
		70	261.56	261.38	261.39	258.73	4.42	262.04	261.90	261.91	258.87	4.28

577 Table 1. Comparison between thermodynamic wet bulb temperatures in the environment far away from the droplet
 578 ($T_{WB\infty}$), simulated droplet steady-state temperatures from Roy et al., (2023) (T_{RRD}), slope transition point temperatures
 579 (T_s), and droplet temperatures at the end of their lifetimes from this study (T_L), in K, for initial droplet radii, $r_0 = 10, 30$ and
 580 $50 \mu\text{m}$, relative humidities, $RH_\infty = 10, 40, 70\%$, and pressures, $P = 500$ and 850 hPa, and ambient temperature, $T_\infty = 273.15$
 581 K (0°C), 268.15 K (-5°C) and 263.15 K (-10°C).
 582



583
 584 Figure 9: Same as Fig. 8 but for $T_\infty = 268.15$ K (-5°C).

585



586
587 **Figure 10: Same as Fig. 8 but for $T_\infty = 263.15$ K (-10°C).**

588
589 **4.3.4 Effect of Ambient Pressure, P**

590 The spatiotemporal evolution of the temperature and droplet radius of an evaporating droplet were also investigated
591 for a higher ambient pressure, $P = 850$ hPa. For a higher pressure, the corresponding decreases in droplet temperatures
592 are smaller and droplet lifetimes are longer. Under the same environmental conditions but with an increase in ambient
593 pressure, water vapor diffusivity decreases, leading to a decreased evaporation rate, reduced cooling, and extended
594
595

T_{∞} (K)	r_0 (μm)	RH_{∞} (%)	$P = 500 \text{ hPa}$				$P = 850 \text{ hPa}$			
			t_{LC} (s)	t_{RRD} (s)	t_L (s)	$\frac{t_L - t_{LC}}{t_{LC}} \times 100\%$	t_{LC} (s)	t_{RRD} (s)	t_L (s)	$\frac{t_L - t_{LC}}{t_{LC}} \times 100\%$
273.15 (0°C)	10	10	0.26	0.56	0.87	234.62	0.44	0.77	1.11	152.27
		40	0.39	0.89	1.51	287.18	0.66	1.18	1.79	171.21
		70	0.78	1.86	3.36	430.77	1.33	2.43	3.87	190.98
	30	10	2.34	5.02	9.54	307.69	3.98	6.84	11.63	192.21
		40	3.51	7.94	16.68	375.21	5.97	10.59	19.33	223.79
		70	7.03	16.73	37.26	430.01	11.95	21.83	42.30	253.97
	50	10	6.51	13.95	27.43	321.35	11.06	19.06	33.35	201.54
		40	9.76	22.08	48.04	392.21	16.59	29.45	55.78	236.23
		70	19.52	46.46	107.45	450.46	33.18	60.64	121.70	266.79
268.15 (-5°C)	10	10	0.38	0.72	1.05	176.32	0.65	1.01	1.32	103.08
		40	0.58	1.12	1.77	205.17	0.98	1.54	2.15	119.39
		70	1.15	2.31	3.91	240	1.96	3.14	4.60	134.69
	30	10	3.45	6.42	11.40	230.43	5.87	9.03	14.27	143.10
		40	5.18	10.01	19.35	273.55	8.81	13.83	23.32	164.70
		70	10.36	20.81	42.79	313.03	17.61	28.25	50.15	184.78
	50	10	9.59	17.88	32.76	241.61	16.31	25.15	40.99	151.32
		40	14.39	27.86	55.76	287.49	24.46	38.48	67.02	173.99
		70	28.78	57.80	123.10	327.73	48.92	78.48	144.07	194.50
263.15 (-10°C)	10	10	0.57	0.95	1.29	126.34	0.98	1.37	1.68	71.43
		40	0.86	1.45	2.13	147.67	1.47	2.08	2.68	82.31
		70	1.72	2.98	4.60	167.44	2.93	4.21	5.66	93.17
	30	10	5.17	8.47	13.95	169.83	8.80	12.28	17.99	104.43
		40	7.76	13.05	23.08	197.42	13.19	18.67	28.83	118.57
		70	15.52	26.79	50.12	222.94	26.39	37.85	61.04	131.29
	50	10	14.37	23.59	40.11	179.12	24.43	34.19	51.59	111.17
		40	21.56	36.30	66.42	208.07	36.65	51.93	82.53	125.18
		70	43.12	74.43	144.33	234.72	73.30	105.16	175.50	139.43

596

597

598 **Table 2: Comparison between different timescales (in sec) in this and other studies, all for the cut off radii used in this**
599 **study. These include droplet lifetimes using the Maxwellian diffusion-limited evaporation approach (t_{LC}), the bulk droplet**
600 **approach in Roy et al., (2023) (t_{RRD}), and as calculated from this study (t_d), for initial droplet radii ($r_0 = 10, 30$ and $50 \mu\text{m}$),**
601 **relative humidities ($RH_\infty = 10, 40, 70\%$), and pressures ($P = 500$ and 850 hPa), and ambient temperature, $T_\infty = 273.15$ K**
602 **(0°C), 268.15 K (-5°C) and 263.15 K (-10°C).**
603

604 droplet lifetimes. For example, for an environment with $T_\infty = 273.15$ K (0°C), $P = 850$ hPa, $10, 30$ and $50 \mu\text{m}$ droplets
605 reach 249.0 K, 261.4 K, and 268.3 K for $RH_\infty = 10\%$, 40% and 70% , respectively, which are slightly higher as
606 compared to the corresponding droplet temperatures (247.3 K, 261.1 K, and 268.2 K) for $P = 500$ hPa (Table 1). For
607 higher ambient pressures, droplet lifetimes are also increased due to reduced evaporation rate, with $50 \mu\text{m}$ droplets
608 now surviving for 33.4 s, 55.8 s, and 121.7 s at $P = 850$ hPa, instead of 27.4 s, 48.0 s, 107.5 s for $P = 500$ hPa for RH_∞
609 $= 10\%$, 40% and 70% , respectively (Table 2). Similar trends can also be observed for lower ambient temperatures,
610 268.15 K and 263.15 K, as shown in Table 2.

611

612 **5 Discussion**

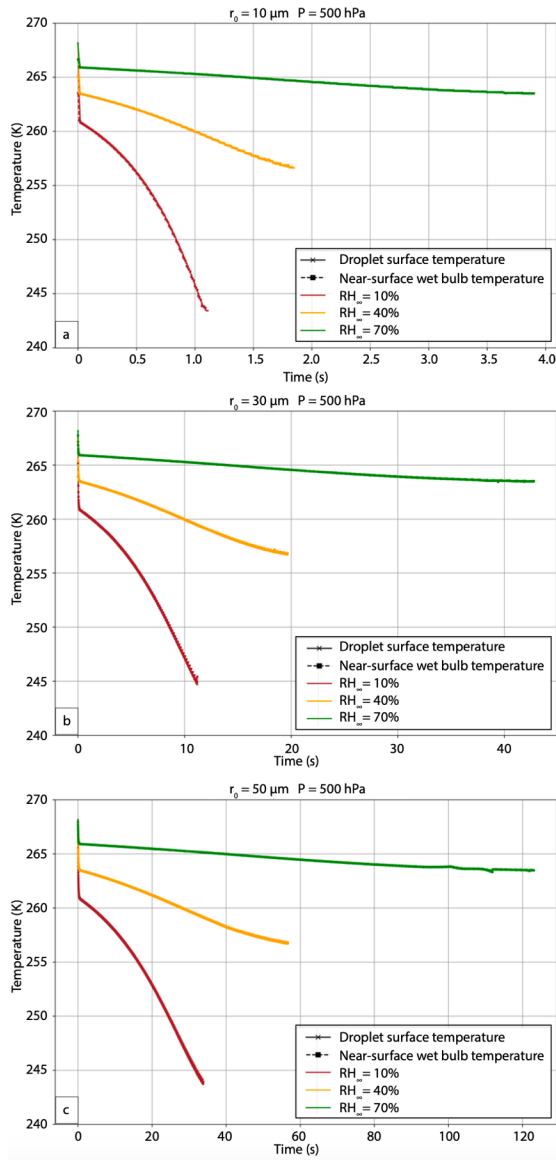
613

614 **5.1 Droplet Temperature Sensitivities and Relationship to Thermodynamic Wet-bulb Temperature**

615

616 In these experiments, the droplet temperature initially rapidly decreases to the thermodynamic wet-bulb temperature
617 of the far environment. The novel finding from this study is that the droplet temperature continues to decrease beyond
618 the thermodynamic wet-bulb temperature of the far environment because of the non-equilibrium condition of the
619 thermal and vapor fields during the evaporation process (Fig. 11). The droplet temperature continues to conform to
620 the wet-bulb temperature directly adjacent to the droplet surface, which is lower than the wet-bulb temperature of the
621 far environment. Note that the dependence on T_∞ and P is much smaller than that on RH_∞ . The strong dependence on
622 RH_∞ compared to temperature results from the initial conditions. The droplet temperature initially is in thermal
623 equilibrium with its environment (the droplet has the same temperature as that of the far environment), but the vapor
624 field is far from equilibrium, especially for low relative humidity environments. As a result, the vapor diffusion rate
625 (which depends on the vapor density gradient) far exceeds the thermal diffusion rate (which depends on the
626 temperature gradient). Because the cloud droplets are small, and the relative humidity gradients are large, the droplets
627 never come to an equilibrium state before evaporating completely into the subsaturated air. The water vapor flux into
628 the larger subsaturated environment maintains a vapor density near the droplet surface that approaches but never
629 reaches saturation. As a result, the wet-bulb temperature near the droplet surface continues to fall but at a slower rate
630 that depends on RH_∞ (Fig. 11). The pressure affects both the moisture and temperature diffusion fluxes, so these scale
631 with each other, resulting in pressure not having a strong effect compared to that of the moisture gradient.

632

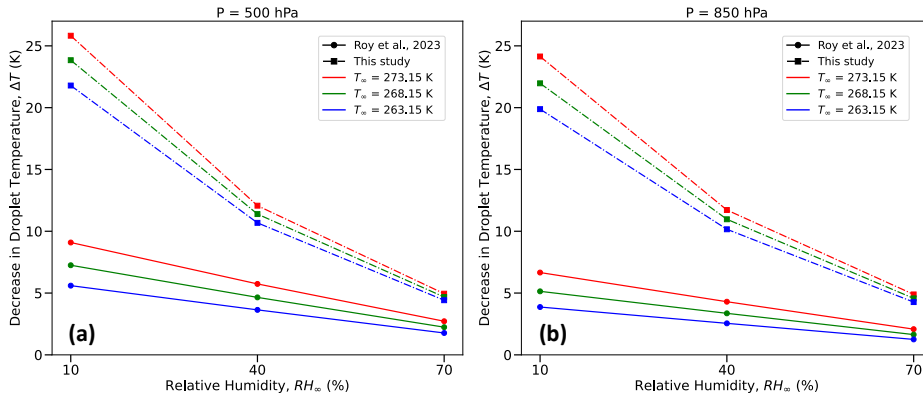


633
 634
 635
 636
 637
 638

Figure 11: Evolution of droplet surface temperature (in K, solid lines with cross symbols), and near-surface thermodynamic wet-bulb temperature (in K, dashed lines with square symbols) for (a) 10, (b) 30 and (c) 50 μm droplet, immersed in an environment with $T_\infty = 268.15$ K (-5°C), $P = 500$ hPa, and three different RH_∞ . The lines representing droplet surface temperature and near-surface thermodynamic wet-bulb temperature essentially overlap.

639 **5.2 Droplet Temperature and Lifetime Comparison with Previous Studies**

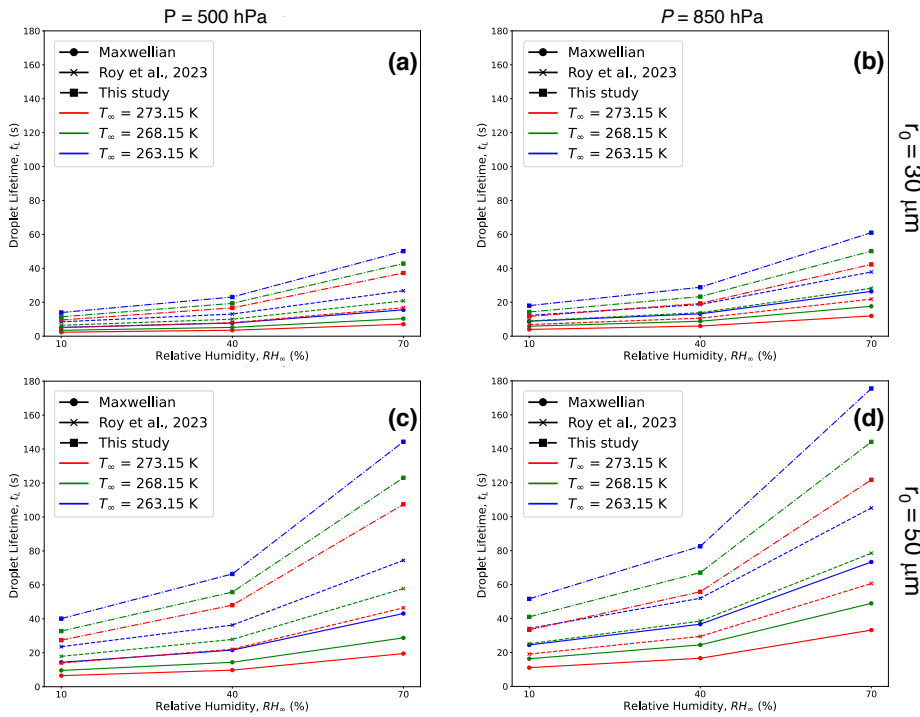
640
 641 As noted in the introduction, not many studies in the cloud microphysics literature have taken a close look at the
 642 explicit numerical estimation of supercooled, evaporating cloud droplet temperatures for a wide range of
 643 environmental conditions. Previously, a study by Srivastava and Coen (1992) investigated the evaporation of isolated,
 644 stationary droplets by iteratively solving the steady-state solutions, using saturation vapor pressure relations from
 645 Wexler (1976) to calculate saturation vapor density, and assumed the heat storage terms in the droplet heat budget to
 646 be negligible. Roy et al., (2023), solving for time-dependent heat and mass transfer between single, stationary cloud
 647 droplets evaporating in infinitely large, prescribed ambient environments, demonstrated that the temperatures of the
 648 cloud droplets reach steady-state quite quickly (< 0.3 s). Their steady-state droplet temperatures agreed well with those
 649 of Srivastava and Coen (1992) and could be approximated by the thermodynamic wet-bulb temperature of the ambient
 650 environment. The current study advances the idealized framework of droplet evaporation as described in Roy et al.,
 651 (2023) by including the impact of internal heat gradients within the droplet and resolving the spatiotemporally
 652 evolving thermal and vapor density gradients between the droplet and its immediate environment to estimate the
 653 evaporating droplet temperature and lifetime with higher accuracy.



654
 655 **Figure 12: Comparison between the decrease in droplet temperatures (in K) from an initial temperature the same as T_∞ ,**
 656 **calculated using the bulk droplet model from Roy et al., (2023) (dashed lines), and this study (dashed-dotted lines), for**
 657 **initial droplet radii, $r_0 = 10, 30$ or $50 \mu\text{m}$, relative humidities ($RH_\infty = 10, 40, 70 \%$), and pressures, $P = 500 \text{ hPa}$ (left column),**
 658 **and 850 hPa (right column), and $T_\infty = 273.15 \text{ K}$ (0°C , red), 268.15 K (-5°C , green) and 263.15 K (-10°C , blue).**

659 Table 1 provides a comparison between thermodynamic wet bulb temperatures of the initial environment ($T_{WB\infty}$),
 660 simulated droplet steady-state temperatures from Roy et al. (2023) (T_{RRD}), and droplet temperatures at the end of their
 661 lifetimes from this study (T_L), in K for several environments. Interestingly, the temperatures at the slope transition
 662 point, T_i , as defined in Sec. 3e, are in excellent agreement with $T_{WB\infty}$ and T_{RRD} . In the current study, the droplet
 663 temperature continues to decrease almost steadily as the immediate environment in the vicinity of the droplet cools,
 664 finally reaching T_L , unlike the evaporating droplet achieving a steady-state temperature in a prescribed ambient
 665 environment far away from the droplet in Roy et al., (2023). The evaporating droplet temperature essentially keeps

666 adjusting to the thermodynamic wet-bulb temperature of its immediate changing environment. Therefore, the more
 667 realistic simulations of evaporating cloud droplets that include the effect of spatiotemporally varying ambient air
 668 thermal and vapor density gradients, as shown in this study, reveal that droplets can potentially achieve even lower
 669 temperatures than previously known or estimated from past studies (Srivastava and Coen, 1992; Roy et al., 2023). The
 670 decrease in droplet temperatures from their initial temperatures can be much larger, especially for drier environments,
 671 as much as 25.8 K for $RH_\infty = 10\%$ and 5.0 K for $RH_\infty = 70\%$, for an environment with $P = 500$ hPa, and $T_\infty = 273.15$
 672 K (Table 1 and Fig. 12a). As shown in Fig. 12, the magnitude of reduction in droplet temperatures decreases with
 673 higher ambient RH_∞ and P , and lower T_∞ , similar to previous studies (Srivastava and Coen, 1992; Roy et al., 2023).



674
 675 **Figure 13: Comparison between droplet lifetimes (as defined in this study) calculated using the Maxwellian diffusion-limited**
 676 **evaporation approach (solid lines), bulk droplet model from Roy et al., (2023) (dashed lines), and this study (dashed-dotted**
 677 **lines), for initial droplet radii, $r_0 = 30 \mu\text{m}$ (upper panel), and $50 \mu\text{m}$ (lower panel), relative humidities ($RH_\infty = 10, 40, 70\%$),**
 678 **and pressures, $P = 500$ hPa (left column), and 850 hPa (right column), and ambient temperature, $T_\infty = 273.15$ K (0°C , red),**
 679 **268.15 K (-5°C , green) and 263.15 K (-10°C , blue). $10 \mu\text{m}$ droplets (not shown here) have much smaller lifetimes compared to**
 680 **30 and $50 \mu\text{m}$ droplets.**

681 Table 2 and Fig. 13 provide comparisons between 10, 30 and 50 μm droplet lifetimes (as defined earlier in Sec. 3a)
 682 using the Maxwellian pure-diffusion-limited evaporation approach (t_{LC}), which ignores evaporative cooling at the
 683 droplet surface (Maxwell, 1890; Eq 13-10 of Pruppacher and Klett, 1997), the “bulk” droplet approach as described
 684 in Roy et al., (2023) (t_{RDD}), which ignores internal droplet heat transfer and spatiotemporally varying thermal and

685 moisture gradients in the ambient air, and results from this study (t_L). The magnitude of t_L is greater than the
686 corresponding values of t_{LC} and t_{RRD} . This is because the droplet temperatures in this study never reach steady-state,
687 and are much lower than the corresponding droplet temperatures from the diffusion-limited approach ($\sim T_\infty$), and Roy
688 et al., (2023) ($\sim T_{RRD}$). The greater decrease in evaporating droplet temperature leads to a greater reduction in saturation
689 vapor pressure at the droplet surface. This results in a slower droplet evaporation rate, therefore increasing the droplet
690 lifetime. As shown in Fig. 13, the increase in droplet lifetime depends on the environmental subsaturation, ambient
691 temperatures, and pressures, with a greater increase for more humid, higher pressure, and lower ambient temperature
692 environments. The increase in droplet lifetimes can potentially enhance ice nucleation by increasing the chances of
693 activation of ice nucleating particles (INPs) within the supercooled cloud droplets (see Sect. 5.3).

694

695 5.3 Implications for ice nucleation

696

697 Ice nucleation rates are influenced by temperature (Wright and Petters, 2013; Kanji et al., 2017) and time (Vali, 1994).
698 There are two theories in ice nucleation modeling: the time-independent "singular hypothesis," which suggests
699 instantaneous ice formation, and the time-dependent "stochastic hypothesis," which proposes that ice clusters in
700 embryos form and vanish continually, with a frequency that depends on temperature. Supercooled cloud droplet
701 temperatures and their lifetimes are potential contributing factors for the enhancement of ice formation within
702 evaporating regions of clouds such as cloud-tops and edges. As discussed in Roy et al., (2023), evaporative cooling
703 of supercooled cloud droplets in subsaturated environments can enhance ice nucleation near cloud boundaries in two
704 ways: by instantly increasing ice-nucleating particle activation due to lower droplet temperatures (consistent with the
705 singular hypothesis) and/or by extending supercooled droplet lifetimes, allowing more time for nucleation events
706 (consistent with the stochastic hypothesis). Based on limited laboratory investigations available on time dependency
707 of heterogeneous ice nucleation, conducted between temperatures -14 and -30 °C, varying fractions of the droplets
708 were reported to freeze within a range of 1 s to 500 s (Welti et al., 2012; Broadley et al., 2012; Murray et al., 2012;
709 Jakobsson et al., 2022).

710

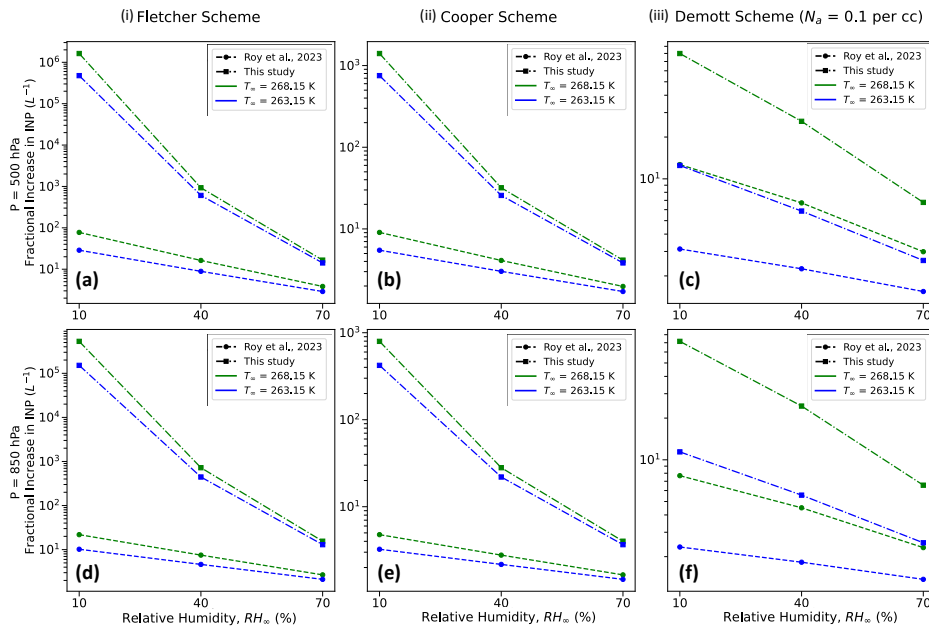
711 Droplet freezing events can potentially occur within the time frame when the evaporating cloud droplets reach lower
712 temperatures due to evaporative cooling before they completely dissipate into the subsaturated air. This can be seen
713 by comparing the values in Table 2 and Fig. 13 with reported droplet freezing timescales available from experimental
714 studies. Droplet lifetimes as estimated from both approaches (t_{RRD} and t_L), which include droplet evaporative cooling,
715 are longer as compared to the Maxwellian diffusion-limited evaporation approach (t_{LC}), allowing more time for
716 potential occurrence of an ice nucleation event. For temperatures between -5 °C and -10 °C, for the three different
717 subsaturated environments ($RH_\infty = 10, 40, \text{ and } 70\%$) examined in this analysis, t_{RRD} typically ranged from 0.7 - 4.2 s
718 for 10 μm , 6-38 s for 30 μm and 18-105 s for 50 μm initial radius of droplets, respectively. For similar environments,
719 $t_L > t_{RRD} > t_{LC}$, with t_L typically ranging from 1.1-5.7 s for 10 μm , 11-61 s for 30 μm and 33-176 s for 50 μm initial
720 radii droplets, respectively. For larger droplets, say 30 and 50 μm , the droplets survive much longer as compared to
721 10 μm droplets, likely enhancing the chances of an ice nucleation event.

722
723 Results from this study further strengthen evidence of the hypothesized mechanism of enhancement of ice nucleation
724 via droplet evaporation. Together with the consistent observation of supercooled water in cloud-top generating cells
725 (Plummer et al., 2014; Zaremba et al., 2024), these results contribute to explaining the observations of the prodigious
726 production of ice particles produced in generating cells at the cloud-tops of winter storms and other clouds (e.g.,
727 Plummer et al., 2015; Wang et al., 2020). Rauber et al. (1986), Plummer et al. (2015), and Tessendorf et al. (2024)
728 have shown that cloud droplet concentrations at the generating cell level near cloud-tops are of the order of 30-50 cm⁻³,
729 while ice-particle concentrations in the plumes of ice particles falling beneath generating cells are of the order of
730 0.01 cm⁻³. Based on these values, if less than one frozen cloud droplet in 1000 survive sublimation after freezing and
731 fall back into the cloud, that would be sufficient to create the ice-particles observed falling from a generating cell.

732
733 Due to the observational evidence of a higher dependency of ice nucleation on temperature than time (Wright and
734 Petters, 2013), and the increased difficulty of representing time-dependent stochastic nucleation in numerical models,
735 the simpler and more widely used approach is to use the time-dependent singular hypothesis framework to simulate
736 ice initiation processes. Drawing from theoretical insights, laboratory experiments, and field campaigns, numerous
737 parameterization methods for modeling heterogeneous ice nucleation in cloud and climate models have been created
738 over the years (Fletcher, 1962; Cooper, 1986; Meyers et al., 1992; DeMott et al., 1998; Khvorostyanov and Curry,
739 2000; Phillips et al., 2008). Most of the conventionally used schemes (Fletcher, 1962; Cooper, 1986; Demott et al.,
740 2010) share a common feature, which is the utilization of the ambient air temperature for estimating activated INPs,
741 as opposed to relying on the droplet temperature, even for primary ice-nucleation modes such as immersion freezing
742 and contact nucleation.

743
744 Similar to Roy et al. (2023), we investigate the maximum enhancement in activated INP concentrations that can occur
745 due to evaporative cooling of supercooled water droplets in a spatiotemporally varying environment, assuming that
746 the activation in the parameterization schemes (Fletcher, 1962; Cooper, 1986; Demott et al., 2010) is related to the
747 droplet temperatures towards the end of their lifetimes (T_L) rather than the ambient temperature. Fig. 14 presents a
748 comparison between Roy et al. (2023), and the current study in terms of the highest fractional increase in activated
749 ice-nucleating particles (INPs), as projected through the Fletcher, Cooper, and Demott schemes (considering ambient
750 aerosol concentration, N_a , with diameters greater than 0.5 μm). Owing to even lower droplet temperatures during
751 evaporation, the fractional increase in activated INPs is higher as calculated from this study, with several orders of
752 magnitude increase for drier environments. For example, the Fletcher Scheme predicts an enhancement in activated
753 INPs by a factor of $\sim 10^6$ for $RH_\infty = 10\%$, $T_\infty = 268.15\text{ K}$, $P = 500\text{ hPa}$ based on droplet temperatures from this study,
754 while the corresponding number from Roy et al. (2023) is ~ 100 (Fig. 14a). The fractional increases are slightly smaller
755 for higher pressure environments due to lower evaporative cooling of the droplets under such conditions (compare
756 Figs. 14a, d, b,e, and c,f). Consistent with previous results from Roy et al. (2023), compared to the Fletcher Scheme,
757 the Cooper and Demott schemes demonstrate relatively lower enhancement in activated INPs. For the same

758 environment stated earlier, the corresponding activated INP enhancement factor values for Cooper and Demott
 759 schemes are $\sim 10^3$ and 80, respectively (Figs. 14b and c).
 760
 761 Therefore, results from the current study further corroborate the hypothesized ice nucleation enhancement mechanism
 762 through evaporative cooling of supercooled droplets (Mossop et al., 1968; Young, 1974; Beard, 1992; Roy et al.,
 763 2023), providing much higher estimates of activated INP concentrations from previous analyses (Roy et al., 2023).
 764 This potential increase in INP concentrations in subsaturated environments near cloud tops and edges, particularly at
 765 higher sub-freezing temperatures, may partially help resolve the several orders of magnitude discrepancy between
 766 predicted INP and observed ice particle concentrations in such regions of the cloud. To evaluate the effectiveness of
 767 the potential ice-nucleation enhancement mechanism through evaporation, future modeling experiments within a
 768 robust dynamical model setup, considering a population of both freezing and evaporating droplets, along with their
 769 lifetimes, droplet-droplet interaction, different species of INPs, and the impact of turbulence and other feedbacks, are
 770 required.



771
 772 **Figure 14: Comparison between the maximum fractional increase in INPs as estimated by Roy et al., (2023) and this study**
 773 **for three different parameterization schemes: (i) Fletcher (1962) (ii) Cooper (1986), and (iii) Demott et al., (2010), for three**
 774 **different environmental relative humidities ($RH_\infty = 10, 40$ and 70%), and two ambient temperatures ($T_\infty = 268.15$ K (-5°C)**
 775 **and 263.15 K (-10°C)) and two different pressures ($P = 500$ and 850 hPa).**

776
 777
 778

779 **6 Conclusions**

780

781 In this study, we presented a quantitative investigation of the temperature and lifetime of an evaporating droplet,
782 considering internal thermal gradients within the droplet as well as resolving spatiotemporally varying **unsteady**
783 thermal and vapor density gradients in the surrounding ambient air. The computational approach involved solving the
784 Navier-Stokes and continuity equations, coupled with heat and vapor diffusion equations, using an advanced
785 numerical model that employs the finite element method. This is the first simulation of the spatiotemporal evolution
786 of droplet temperature, radius, and its environment for an isolated, stationary, and supercooled cloud droplet
787 evaporating in various subsaturated environmental conditions. Various ambient pressure (P), temperature (T_∞),
788 relative humidity (RH_∞), and initial droplet radii (r_0) were considered. The motivation behind this study was to provide
789 more exacting calculations to support the hypothesized ice nucleation enhancement mechanism due to the evaporation
790 of supercooled cloud droplets at cloud boundaries, such as cloud-top ice-generating cells, and for ambient temperatures
791 between 0°C and -10°C where ice nucleation is least effective.

792

793 The numerical simulations show for typical cloud droplet sizes ($r_0 = 10, 30, 50 \mu\text{m}$) and environmental conditions
794 considered here, the internal thermal gradients dissipate quite quickly ($\leq 0.3 \text{ s}$) when the droplet is introduced to a new
795 subsaturated environment. Thus, spatial thermal gradients within the droplet can be reasonably ignored. Hence, one
796 can potentially ignore the extra computational expense of simulating conductive heat transfer within the droplet for
797 timescales $> 1 \text{ s}$.

798

799 The results from this study are similar to findings from the literature that an evaporating supercooled cloud droplet
800 can exist at a temperature lower than that of the ambient atmosphere and that the tendencies of the dependence of
801 decrease in droplet temperatures on environmental factors and initial droplet sizes (Srivastava and Coen, 1992; Roy
802 et. al, 2023). The novelty of this study lies in demonstrating that the magnitude of droplet cooling can be much higher
803 than estimated from past studies of droplet evaporation, especially for drier environments. For example, a droplet
804 evaporating in an environment with $P = 500 \text{ hPa}$, $T_\infty = 268.15 \text{ K}$ (-5°C), $RH_\infty = 10\%$, Roy et al., (2023) estimated a
805 7.3 K decrease in droplet temperature, while this study shows that there can be as much as a 23.8 K decrease in droplet
806 temperature. This is because previous studies assumed prescribed ambient environments at all distances from the
807 droplet, while this analysis shows that as a droplet evaporates and cools, the air in the vicinity of the droplet cools as
808 well, giving rise to spatiotemporally varying thermal and vapor density fields in the immediate environment
809 surrounding the droplet. Here, the net conductive warming from the environmental air enveloping the droplet is lower
810 as compared to Roy et al., (2023), effectively leading to a much lower droplet temperature. At a particular time, the
811 strength and radial dependence of these gradients depend on the subsaturation of the air medium and the magnitude
812 of droplet cooling due to evaporation, with the largest cooling at lower RH_∞ . In this study, the temperature and vapor
813 density in the ambient air continually evolve, thus affecting the transfer of heat and vapor between the droplet surface
814 and the environment far away from the droplet. This affects the temperature evolution and decay rates of the

815 evaporating droplet to a greater degree than shown in previous studies for a similar environment (Srivastava and
816 Cohen, 1992; Roy et al. 2023).

817
818 This study also demonstrated that the lifetimes of the evaporating droplets are longer compared to Roy et al. (2023)
819 because as the droplet temperature gets lower, the saturation vapor pressure at the droplet surface reduces, leading to
820 a weaker evaporation rate. For an environment with $P = 500$ hPa, $T_{\infty} = 268.15$ K (-5°C), $RH_{\infty} = 10\%$, a $50\ \mu\text{m}$ droplet
821 reaches the end of its lifetime, as defined in this study, in 32.8s, while the corresponding values for the diffusion-
822 limited evaporation approach as estimated from Roy et. al, (2023) are 9.6 s and 17.9 s, respectively. The rates of
823 evaporation tend to be lower in this study due to even lower droplet temperatures as well as spatiotemporally varying
824 vapor density gradients around the droplets. As the droplet evaporates, the envelope of air surrounding the droplet is
825 colder, has lower values of diffusivity leading to lower evaporation rates, and has higher vapor concentration than the
826 ambient air, thus decreasing the evaporation rates.

827
828 To summarize, if one considers the more realistic case of droplet evaporation, including the spatiotemporally varying
829 thermal and vapor density gradients in the vicinity of the water droplet, the evaporating droplet can experience a
830 substantial reduction in temperatures by several degrees, strongly dependent on the ambient relative humidity and
831 weakly dependent on ambient pressure and temperature. Similar to the case of an isolated, stationary droplet
832 evaporating in a prescribed ambient environment, the droplet almost immediately reaches its slope transition point
833 temperature, which can be well-approximated by the thermodynamic wet-bulb temperature of the initial ambient
834 environment around the droplet. Droplet temperatures then continue to steadily decrease as they adjust to the evolving
835 thermodynamic wet-bulb temperature of the surrounding air. In more humid environments, the droplets may not
836 experience a larger droplet cooling, but their lifetimes, as defined in this study, get extended by tens of seconds as
837 compared to the Maxwellian estimation which neglects droplet cooling.

838
839 The current analysis also demonstrates that lower evaporating droplet temperatures would lead to an enhancement of
840 activated INPs from three widely used INP parameterization schemes, further corroborating the hypothesized ice
841 nucleation enhancement mechanism through evaporative cooling of supercooled droplets. Notably, the estimates of
842 activated INP concentrations from this study are higher than previous analyses, as the droplet temperatures are much
843 lower towards the end of their lifetimes, with several orders of magnitude increase in activated INPs for drier
844 environments. The Fletcher Scheme predicts the greatest enhancement in activated INPs by a factor of $\sim 10^6$ for RH_{∞}
845 $= 10\%$, $T_{\infty} = 268.15$ K, $P = 500$ hPa, while the corresponding enhancement factor values for Cooper and Demott
846 schemes are $\sim 10^3$ and 80, respectively.

847
848 This study suggests a need for a more in-depth examination of supercooled cloud droplet temperatures and their
849 lifetimes in subsaturated environments, especially when simulating heterogeneous ice nucleation processes that
850 require the presence of supercooled water droplets. This is crucial because the concentration of activated ice-
851 nucleating particles (INPs) is influenced by both droplet temperature and how long evaporating droplets persist.

852 Additionally, the findings from this investigation may also partially help understand disparities between observed ice
853 particle concentrations and activated INPs, especially at relatively higher sub-0°C temperatures. Including the effect
854 of droplet evaporative cooling on droplet temperatures and lifetimes, while modeling cloud microphysical processes
855 in subsaturated environments, will also lead to improved accuracy of the evolution of the droplet size distribution as
856 well as primary ice nucleation mechanisms.

857
858 **Author contribution:** PR, RMR and LDG conceptualized the problem and numerical experiments. PR designed and
859 performed the simulations, analyzed the data, and prepared the first draft of the manuscript. RMR and LDG reviewed
860 and edited the manuscript. RMR and LDG acquired required funding for the project.

861
862 **Competing interests:** The authors have no competing interests.

863
864 **Acknowledgements:** This work was funded by the NASA CAMP²Ex program under grant 80NSSC18K0144 and the
865 NASA Earth Venture Suborbital-3 (EVS-3) IMPACTS program under grant 80NSSC19K0355. This research was
866 also supported by the National Science Foundation under grant NSF AGS-2016106.

867
868 **Code/Data availability:** This modeling analysis used the proprietary COMSOL Multiphysics version 6.0 software
869 package which can be licensed through <https://www.comsol.com/>.

870 References

- 871
872
873 Alduchov, O.A. and Eskridge, R.E.: Improved Magnus form approximation of saturation vapor pressure, *Journal of*
874 *Applied Meteorology and Climatology*, 35(4), pp.601-609, [https://doi.org/10.1175/1520-](https://doi.org/10.1175/1520-0450(1996)035<0601:IMFAOS>2.0.CO;2)
875 [0450\(1996\)035<0601:IMFAOS>2.0.CO;2](https://doi.org/10.1175/1520-0450(1996)035<0601:IMFAOS>2.0.CO;2), 1996.
- 876 American Meteorological Society (AMS 2024): Generating cell. https://glossary.ametsoc.org/wiki/Generating_cell
877 (Last accessed May 10, 2024)
- 878 Beard, K.: Ice Initiation in warm-base convective clouds: An assessment of microphysical mechanisms, *Atmos. Res.*,
879 28, 125-152, [https://doi.org/10.1016/0169-8095\(92\)90024-5](https://doi.org/10.1016/0169-8095(92)90024-5), 1992.
- 880 Biddle, J.W., Holten, V., Sengers, J.V. and Anisimov, M.A.: Thermal conductivity of supercooled water. *Physical*
881 *Review E*, 87(4), p.042302, <https://doi.org/10.1103/PhysRevE.87.042302>, 2013.
- 882 Broadley, S.L., Murray, B.J., Herbert, R.J., Atkinson, J.D., Dobbie, S., Malkin, T.L., Condiliffe, E. and Neve, L.:
883 Immersion mode heterogeneous ice nucleation by an illite rich powder representative of atmospheric mineral
884 dust_ *Atmospheric Chemistry and Physics*, 12(1), pp.287-307, <https://doi.org/10.5194/acp-12-287-2012>,
885 2012.
- 886 [Chen, S., Xue, L. and Yau, M.K.: Impact of aerosols and turbulence on cloud droplet growth: an in-cloud seeding case](#)
887 [study using a parcel–DNS \(direct numerical simulation\) approach, *Atmospheric Chemistry and Physics*,
888 \[20\\(17\\), pp.10111-10124. <https://doi.org/10.5194/acp-20-10111-2020>, 2020.\]\(#\)](#)

890 Chushak, Y.G. and Bartell, L.S.: Simulations of spontaneous phase transitions in large, deeply supercooled clusters
891 of SeF₆, *The Journal of Physical Chemistry B*, 103(50), pp.11196-11204, <https://doi.org/10.1021/jp992818g>,
892 1999.

893 Chushak, Y. and Bartell, L.S.: Crystal nucleation and growth in large clusters of SeF₆ from molecular dynamics
894 simulations, *The Journal of Physical Chemistry A*, 104(41), pp.9328-9336,
895 <https://doi.org/10.1021/jp002107e>, 2000.

896 COMSOL 2023a Cylindrical System Documentation, Last Accessed Sept 15, 2023
897 https://doc.comsol.com/5.5/doc/com.comsol.help.comsol/comsol_ref_definitions.12.090.html

898 COMSOL 2023b Infinite Element Domain Documentation, Last Accessed Sept 15, 2023
899 https://doc.comsol.com/5.5/doc/com.comsol.help.comsol/comsol_ref_definitions.12.116.html

900 COMSOL 2023c Free Triangular Documentation, Last Accessed Sept 15, 2023
901 https://doc.comsol.com/5.5/doc/com.comsol.help.comsol/comsol_ref_mesh.15.38.html

902 COMSOL 2023d Mapped Documentation, Last Accessed Sept 15, 2023
903 https://doc.comsol.com/5.6/doc/com.comsol.help.comsol/comsol_ref_mesh.20.40.html

904 Cooper, W.A.: Ice initiation in natural clouds. In *Precipitation enhancement—A scientific challenge* (pp. 29-32).
905 American Meteorological Society, Boston, MA, <https://doi.org/10.1175/0065-9401-21.43.29>, 1986.

906 DeMott, P.J., Rogers, D.C., Kreidenweis, S.M., Chen, Y., Twohy, C.H., Baumgardner, D., Heymsfield, A.J. and Chan,
907 K.R.: The role of heterogeneous freezing nucleation in upper tropospheric clouds: Inferences from
908 SUCCESS, *Geophysical Research Letters*, 25(9), pp.1387-1390, <https://doi.org/10.1029/97GL03779>, 1998.

909 DeMott, P.J., Prenni, A.J., Liu, X., Kreidenweis, S.M., Petters, M.D., Twohy, C.H., Richardson, M.S., Eidhammer,
910 T. and Rogers, D.: Predicting global atmospheric ice nuclei distributions and their impacts on
911 climate, *Proceedings of the National Academy of Sciences*, 107(25), pp.11217-11222,
912 <https://doi.org/10.1073/pnas.0910818107>, 2010.

913 Djikaev, Y.S., Tabazadeh, A., Hamill, P. and Reiss, H.: Thermodynamic conditions for the surface-stimulated
914 crystallization of atmospheric droplets, *The Journal of Physical Chemistry A*, 106(43), pp.10247-10253,
915 <https://doi.org/10.1021/jp021044s>, 2002.

916 Djikaev, Y.S. and Ruckenstein, E.: Thermodynamics of heterogeneous crystal nucleation in contact and immersion
917 modes, *The Journal of Physical Chemistry A*, 112(46), pp.11677-11687, <https://doi.org/10.1021/jp803155f>,
918 2008.

919 Fletcher, N.H.: *The physics of rainclouds/NH Fletcher; with an introductory chapter by P. Squires and a foreword by*
920 *EG Bowen*. Cambridge University Press, <https://doi.org/10.1002/qj.49708837821>, 1962.

921 Fukuta, N.: Theories of competitive cloud droplet growth and their application to cloud physics studies, *Journal of*
922 *the Atmospheric Sciences*, 49, 1107–1114, [https://doi.org/10.1175/1520-0469\(1992\)049<1107:TOCCDG>2.0.CO;2](https://doi.org/10.1175/1520-0469(1992)049<1107:TOCCDG>2.0.CO;2), 1992.

924 Grabowski, W.W. and Wang, L.P.: Growth of cloud droplets in a turbulent environment, *Annual Review of Fluid*
925 *Mechanics*, 45, pp.293-324, <https://doi.org/10.1146/annurev-fluid-011212-140750>, 2013.

926 Hall, W.D. and Pruppacher, H.R.: The survival of ice particles falling from cirrus clouds in subsaturated air, *Journal*
927 *of Atmospheric Sciences*, 33(10), pp.1995-2006, [https://doi.org/10.1175/1520-](https://doi.org/10.1175/1520-0469(1976)033<1995:TSOIPF>2.0.CO;2)
928 [0469\(1976\)033<1995:TSOIPF>2.0.CO;2](https://doi.org/10.1175/1520-0469(1976)033<1995:TSOIPF>2.0.CO;2), 1976.

929 Jakobsson, J.K., Waman, D.B., Phillips, V.T. and Bjerring Kristensen, T.: Time dependence of heterogeneous ice
930 nucleation by ambient aerosols: laboratory observations and a formulation for models. *Atmospheric*
931 *Chemistry and Physics*, 22(10), pp.6717-6748, <https://doi.org/10.5194/acp-22-6717-2022>, 2022.

932 Kanji, Z. A., Ladino, L. A., Wex H., Boose, Y., Burkert-Kohn, M., Cziczo, D. J. and Krämer, M.: Overview of Ice
933 Nucleating Particles, *Meteor. Monogr.*, **58**, 1.1–1.33, [https://doi.org/10.1175/AMSMONOGRAPHS-D-16-](https://doi.org/10.1175/AMSMONOGRAPHS-D-16-0006.1)
934 [0006.1](https://doi.org/10.1175/AMSMONOGRAPHS-D-16-0006.1), 2017.

935 Khain, A.P. and Pinsky, M.: Physical processes in clouds and cloud modeling, Cambridge University Press, 2018.

936 Khvorostyanov, V.I. and Curry, J.A.: A new theory of heterogeneous ice nucleation for application in cloud and
937 climate models, *Geophysical Research Letters*, 27(24), pp.4081-4084,
938 <https://doi.org/10.1029/1999GL011211>, 2000.

939 Khvorostyanov, V. and Sassen, K.: Toward the theory of homogeneous nucleation and its parameterization for cloud
940 models, *Geophysical research letters*, 25(16), pp.3155-3158, <https://doi.org/10.1029/98GL02332>, 1998.

941 Kinzer, G. D., and Gunn, R.: The evaporation, temperature and thermal relaxation-time of freely falling waterdrops,
942 *J. Meteor.*, 8, 71–83. [https://doi.org/10.1175/1520-0469\(1951\)008<0071:TETATR>2.0.CO;2](https://doi.org/10.1175/1520-0469(1951)008<0071:TETATR>2.0.CO;2), 1951.

943 Lü, Y.J., Xie, W.J. and Wei, B.: Observation of ice nucleation in acoustically levitated water drops, *Applied Physics*
944 *Letters*, 87(18), <http://dx.doi.org/10.1063/1.2126801>, 2005.

945 Marquis, J. and Harrington, J.Y.: Radiative influences on drop and cloud condensation nuclei equilibrium in
946 stratocumulus, *Journal of Geophysical Research: Atmospheres*, 110(D10),
947 <https://doi.org/10.1029/2004JD005401>, 2005.

948 [Mason, B. J.: *The Physics of Clouds*, Clarendon Press, Oxford, 671pp.1971.](#)

949 Maxwell, J.C.: Theory of the wet bulb thermometer, *Scientific Papers of James Clerk Maxwell*, 2, p.636, 1890.

950 Meyers, M.P., DeMott, P.J. and Cotton, W.R.: New primary ice-nucleation parameterizations in an explicit cloud
951 model, *Journal of Applied Meteorology and Climatology*, 31(7), pp.708-721, [https://doi.org/10.1175/1520-](https://doi.org/10.1175/1520-0450(1992)031<0708:NPINPI>2.0.CO;2)
952 [0450\(1992\)031<0708:NPINPI>2.0.CO;2](https://doi.org/10.1175/1520-0450(1992)031<0708:NPINPI>2.0.CO;2), 1992.

953 Mossop, S.C., Ruskin, R.E. and Heffernan, K.J.: Glaciation of a Cumulus at Approximately– 4C, *Journal of*
954 *Atmospheric Sciences*, 25(5), pp.889-899, [https://doi.org/10.1175/1520-](https://doi.org/10.1175/1520-0469(1968)025<0889:GOACAA>2.0.CO;2)
955 [0469\(1968\)025<0889:GOACAA>2.0.CO;2](https://doi.org/10.1175/1520-0469(1968)025<0889:GOACAA>2.0.CO;2), 1968.

956 Murray, B.J., O'sullivan, D., Atkinson, J.D. and Webb, M.E.: Ice nucleation by particles immersed in supercooled
957 cloud droplets, *Chemical Society Reviews*, 41(19), pp.6519-6554, doi:10.1039/c2cs35200a., 2012.

958 Phillips, V.T., DeMott, P.J. and Andronache, C.: An empirical parameterization of heterogeneous ice nucleation for
959 multiple chemical species of aerosol, *Journal of the Atmospheric Sciences*, 65(9), pp.2757-2783,
960 <https://doi.org/10.1175/2007JAS2546.1>, 2008.

961 Plummer, D.M., McFarquhar, G.M., Rauber, R.M., Jewett, B.F. and Leon, D.C.: Structure and statistical analysis of
962 the microphysical properties of generating cells in the comma head region of continental winter cyclones,
963 *Journal of the Atmospheric Sciences*, 71(11), pp.4181-4203, <https://doi.org/10.1175/JAS-D-14-0100.1>, 2014.

964 Plummer, D. M., G. M. McFarquhar, R. M. Rauber, B. F. Jewett, and Leon., D. C.: Microphysical properties of
965 convectively generated fall streaks in the comma head region of continental winter cyclones, *J. Atmos.*
966 *Sci.*, **72**, 2465–2483, doi:10.1175/JAS-D-14-0354.1, 2015.

967 Pruppacher, H. R., and Klett, J. D.: *Microphysics of Clouds and Precipitation*. 2d ed. Kluwer Academic, 954 pp.,
968 1997.

969 Ramelli, F., Henneberger, J., David, R.O., Bühl, J., Radenz, M., Seifert, P., Wieder, J., Lauber, A., Pasquier, J.T.,
970 Engelmann, R. and Mignani, C.: Microphysical investigation of the seeder and feeder region of an Alpine
971 mixed-phase cloud, *Atmospheric Chemistry and Physics*, 21(9), pp.6681-6706, [https://doi.org/10.5194/acp-](https://doi.org/10.5194/acp-21-6681-2021)
972 [21-6681-2021](https://doi.org/10.5194/acp-21-6681-2021), 2021.

973 Rauber, R. M., Grant, L. O.: The characteristics and distribution of cloud water over the mountains of northern
974 Colorado during winter-time storms. Part II: Spatial distribution and microphysical characteristics. *J.*
975 *Climate Appl. Meteor.*, 25, 489–504, [https://doi.org/10.1175/1520-](https://doi.org/10.1175/1520-0450(1986)025<0489:TCADOC>2.0.CO;2)
976 [0450\(1986\)025<0489:TCADOC>2.0.CO;2](https://doi.org/10.1175/1520-0450(1986)025<0489:TCADOC>2.0.CO;2), 1986.

977 Roach, W. T.: On the effect of radiative exchange on the growth by condensation of a cloud or fog droplet, *Quart. J.*
978 *Roy. Meteor. Soc.*, 102, 361–372, <https://doi.org/10.1002/qj.49710243207>, 1976.

979 Rogers, R.R. and Yau, M.K.: *A Short Course in Cloud Physics*. Pergamon Press, 294 pp., 1989.

980 Rowe, P.M., Fergoda, M. and Neshyba, S.: Temperature-dependent optical properties of liquid water from 240 to 298
981 K. *Journal of Geophysical Research: Atmospheres*, 125(17), <https://doi.org/10.1029/2020JD032624>, 2020.

982 Roy, P., Rauber, R.M. and Girolamo, L.D.: A closer look at the evolution of supercooled cloud droplet temperature
983 and lifetime in different environmental conditions with implications for ice nucleation in the evaporating
984 regions of clouds, *Journal of the Atmospheric Sciences*. <https://doi.org/10.1175/JAS-D-22-0239.1>, 2023.

985 Satoh, I., Fushinobu, K. and Hashimoto, Y.: Freezing of a water droplet due to evaporation—heat transfer dominating
986 the evaporation–freezing phenomena and the effect of boiling on freezing characteristics, *International*
987 *Journal of Refrigeration*, 25(2), pp.226-234, [http://dx.doi.org/10.1016/S0140-7007\(01\)00083-4](http://dx.doi.org/10.1016/S0140-7007(01)00083-4), 2002.

988 Scardovelli, R. and Zaleski, S.: Direct numerical simulation of free-surface and interfacial flow, *Annual review of fluid*
989 *mechanics*, 31(1), pp.567-603. <https://doi.org/10.1146/annurev.fluid.31.1.567>, 1999.

990 Sedunov, Y. S.: *Physics of the Drop Formation in the Atmosphere*, John Wiley and Sons, 234 pp., 1974.

991 Shaw, R.A., Durant, A.J. and Mi, Y.: Heterogeneous surface crystallization observed in undercooled water, *The*
992 *Journal of Physical Chemistry B*, 109(20), pp.9865-9868, <https://doi.org/10.1021/jp0506336>, 2005.

993 Srivastava, R.C. and Coen, J.L.: New explicit equations for the accurate calculation of the growth and evaporation of
994 hydrometeors by the diffusion of water vapor, *Journal of Atmospheric Sciences*, 49(17), pp.1643-1651,
995 [https://doi.org/10.1175/1520-0469\(1992\)049<1643:NEEFTA>2.0.CO;2](https://doi.org/10.1175/1520-0469(1992)049<1643:NEEFTA>2.0.CO;2), 1992.

996 Standard Atmosphere: ISO 2533:1975, updated 2021: <https://www.iso.org/standard/7472.html>, 2021, last accessed
997 09/26/2022.

998 Szakáll, M., Debertshäuser, M., Lackner, C.P., Mayer, A., Eppers, O., Diehl, K., Theis, A., Mitra, S.K. and Borrmann,
999 S.: Comparative study on immersion freezing utilizing single-droplet levitation methods, *Atmospheric*
1000 *Chemistry and Physics*, 21(5), pp.3289-3316, <https://doi.org/10.5194/acp-21-3289-2021>, 2021.

1001 Tabazadeh, A., Djikaev, Y.S., Hamill, P. and Reiss, H.: Laboratory evidence for surface nucleation of solid polar
1002 stratospheric cloud particles, *The Journal of Physical Chemistry A*, 106(43), pp.10238-10246,
1003 <https://doi.org/10.1021/jp021045k>, 2002a.

1004 Tabazadeh, A., Djikaev, Y.S. and Reiss, H.: Surface crystallization of supercooled water in clouds, *Proceedings of*
1005 *the National Academy of Sciences*, 99(25), pp.15873-15878, <https://doi.org/10.1073/pnas.252640699>, 2002b.

1006 Tessendorf, S.A., Boe, B., Geerts, B., Manton, M.J., Parkinson, S. and Rasmussen, R.: The future of winter orographic
1007 cloud seeding: A view from scientists and stakeholders, *Bulletin of the American Meteorological Society*,
1008 96(12), pp.2195-2198, <https://doi.org/10.1175/BAMS-D-15-00146.1>, 2015.

1009 Tessendorf, S., Ikeda, K., Rasmussen, R., French, J., Rauber, R., Korolev, A., Xue, L., Blestrud, D., Dawson, N.,
1010 Meadows, M., Kunkel, M. and Parkinson, S.: Characteristics of Generating Cells in Wintertime Orographic
1011 Clouds. *Journal of the Atmospheric Sciences*, 81(3), pp. 649-673.
1012 <https://journals.ametsoc.org/view/journals/atsc/81/3/JAS-D-23-0029.1.xml>, 2024.

1013 Vaillancourt, P.A., Yau, M.K. and Grabowski, W.W.: Microscopic approach to cloud droplet growth by condensation.
1014 Part I: Model description and results without turbulence, *Journal of the Atmospheric Sciences*, 58(14),
1015 pp.1945-1964, [https://doi.org/10.1175/1520-0469\(2001\)058%3C1945:MATCDG%3E2.0.CO;2](https://doi.org/10.1175/1520-0469(2001)058%3C1945:MATCDG%3E2.0.CO;2), 2001.

1016 Vali, G.: Freezing Rate Due to Heterogeneous Nucleation. *J. Atmos. Sci.*, **51**, 1843–
1017 1856, [https://doi.org/10.1175/1520-0469\(1994\)051<1843:FRDTHN>2.0.CO;2](https://doi.org/10.1175/1520-0469(1994)051<1843:FRDTHN>2.0.CO;2), 1994.

1018 Volmer, M.: *Kinetik der Phasenbildung* (Steinkopff, Dresden, Leipzig), 1939.

1019 Wang, Y., McFarquhar, G.M., Rauber, R.M., Zhao, C., Wu, W., Finlon, J.A., Stechman, D.M., Stith, J., Jensen, J.B.,
1020 Schnaiter, M. and Järvinen, E.: Microphysical properties of generating cells over the Southern Ocean: Results
1021 from SOCRATES, *Journal of Geophysical Research: Atmospheres*, 125(13),
1022 <https://doi.org/10.1029/2019JD032237>, 2020.

1023 Watts, R.G.: Relaxation time and steady evaporation rate of freely falling raindrops, *Journal of Atmospheric Sciences*,
1024 28(2), pp.219-225, [https://doi.org/10.1175/1520-0469\(1971\)028<0219:RTASER>2.0.CO;2](https://doi.org/10.1175/1520-0469(1971)028<0219:RTASER>2.0.CO;2), 1971.

1025 Watts, R.G. and Farhi, I.: Relaxation times for stationary evaporating liquid droplets, *Journal of the Atmospheric*
1026 *Sciences*, 32(9), pp.1864-1867, [https://doi.org/10.1175/1520-0469\(1975\)032%3C1864:RTFSEL%3E2.0.CO;2](https://doi.org/10.1175/1520-0469(1975)032%3C1864:RTFSEL%3E2.0.CO;2), 1975.

1028 Welti, A., Lüönd, F., Kanji, Z.A., Stetzer, O. and Lohmann, U.: Time dependence of immersion freezing: a
1029 experimental study on size selected kaolinite particles. *Atmospheric Chemistry and Physics*, 12(20), pp.9893-
1030 9907, 2012.

1031 Wexler, A.: Vapor pressure formulation for water in range 0 to 1008C. A revision, *J. Res. Natl. Bur. Stand. (U.S.)*,
1032 80A, 775–785, <https://doi.org/10.6028%2Fjres.080A.071>, 1976.

1033 White, F.M.: *Viscous Fluid Flow*, 3rd ed., McGraw-Hill, 2006, 656 pp.

- 1034 Wright, T. P., and Petters, M.D.: The role of time in heterogeneous freezing nucleation, *J. Geophys. Res.*, 118, 3731–
1035 3743, <https://doi.org/10.1002/jgrd.50365>, 2013.
- 1036 Yang, K., Hong, F. and Cheng, P.: A fully coupled numerical simulation of sessile droplet evaporation using Arbitrary
1037 Lagrangian–Eulerian formulation. *International Journal of Heat and Mass Transfer*, 70, pp.409-420,
1038 <https://doi.org/10.1016/j.ijheatmasstransfer.2013.11.017>, 2014.
- 1039 Young, K. C.: The Role of Contact Nucleation in Ice Phase Initiation in Clouds, *Journal of the Atmospheric Sciences*,
1040 31, 768–776,
1041 [https://doi.org/10.1175/1520-0469\(1974\)031<0768:TROCNI>2.0.CO;2](https://doi.org/10.1175/1520-0469(1974)031<0768:TROCNI>2.0.CO;2), 1974.
- 1042 Zaremba, T.J., Rauber, R.M., Heimes, K., Yorks, J.E., Finlon, J.A., Nicholls, S.D., Selmer, P., McMurdie, L.A. and
1043 McFarquhar, G.M.: Cloud-Top Phase Characterization of Extratropical Cyclones over the Northeast and
1044 Midwest United States: Results from IMPACTS, *Journal of the Atmospheric Sciences*, 81(2), pp.341-361,
1045 <https://doi.org/10.1175/JAMC-D-22-0154.1>, 2024.